A split-explicit second order Runge-Kutta method for solving 3D hydrodynamic equations

Ange Pacifique Ishimwe[a,*], Eric Deleersnijder[b], Vincent Legat[a], Jonathan Lambrechts[a]

[a] *Université catholique de Louvain, Institute of Mechanics, Materials and Civil Engineering (IMMC), Avenue Georges Lemaître 4, B-1348 Louvain-la-Neuve, Belgium*
[b] *Université catholique de Louvain, Institute of Mechanics, Materials and Civil Engineering (IMMC) & Earth and Life Institute (ELI), Avenue Georges Lemaître 4, B-1348 Louvain-la-Neuve, Belgium*

Abstract

Numerical models of marine hydrodynamics have to deal with processes exhibiting a wide range of timescales. These processes include fast external gravity waves and slower internal fully three-dimensional motions. In order to be both time-efficient and numerically stable, the time stepping scheme has to be chosen carefully to cope with the characteristic time scale of each phenomenon. An usual approach is to split the fast and slow dynamics into separate modes. The fast waves are modelled with a two-dimensional system through depth averaging while the other motions, where characteristic times are much longer, are dealt with in three dimensions. However, if the splitting is inexact, for instance in projecting the fields in a new 3D mesh, this procedure can lead to improper results regarding to the physical properties such as mass conservation and tracer consistency. In this work, a new split-explicit Runge-Kutta scheme is adapted and developed for the Discontinuous-Galerkin Finite Element method in order to obtain a new second-order time stepping, yielding to more accurate results. This method combines a three-stage low-storage Runge-Kutta for the slow processes and a two-stage low-storage for the fast ones. The 3D iterations are not affecting the surface elevation, hence an Arbitrary Lagrangian Eulerian implementation is straightforward. Water volume and tracers are conserved. A set of test cases for baroclinic flows as well as a laboratory application demonstrate the performance of the scheme. They suggest that the new scheme has little numerical diffusion.

Keywords: Unstructure mesh, split-explicit Runge-Kutta, hydrodynamic equations, timestep methods

1. Introduction

Numerical simulation allows to understand processes taking place in the marine environment and, to some extent, predict their evolution. Formulating the relevant equations, selecting the values of the parameters and designing the initial and boundary conditions are challenges that have been addressed in various manners (Fringer et al., 2019). Most estuarine, coastal and shelf sea models are based on the hydrostatic and Boussinesq approximations (Pearson et al., 2017). However, for smaller-scale phenomena, the effects of non-hydrostatic equations are sometimes taken into account (Lermusiaux et al., 2013).

Ocean models have to deal with large aspect ratio domains where the horizontal length scales can reach several thousands of kilometers while the depth is generally of the order of one kilometer or smaller. For this reason, various types of spatial and temporal discretizations have been developed which handle separately the horizontal and vertical directions. In the vertical direction, layered meshes, including terrain-following sigma-levels (Blumberg and Mellor, 1987; Pan et al., 2021), z-levels (Griffies et al., 2005) and their generalization (Song and Haidvogel, 1994) are generally used. It is worth mentioning that, in some ocean models, isopycnal coordinates (Bleck and Smith, 1990) are used. In the horizontal direction, a large

*Corresponding author
Email address: ange.ishimwe@uclouvain.be (Ange Pacifique Ishimwe)

number of models (ROMS (Kumar et al., 2012), POM(Weiss et al., 2018), etc.) are based on structured grids, as the associated numerical methods are computationally efficient (Danilov et al., 2008; Blumberg and Mellor, 1987). This distinct advantage is partially offset by a lack of geometrical flexibility (Deleersnijder and Lermusiaux, 2008) to deal with complex topographical features and small-scale localised processes.

As a consequence, models based on horizontally-unstructured meshes are becoming increasingly popular, e.g., FVCOM (Chen et al., 2003), SUNTANS (Fringer et al., 2006), SCHISM (Zhang et al., 2016), FESOM (Scholz et al., 2013). These models use finite volume (e.g. FVCOM) or finite element (e.g. SCHISM) discretizations, or an approach lying in between them, namely the discontinuous Galerkin method e.g. SLIM (Dobbelaere et al., 2022), (Vallaeys et al., 2021). The latter, hereafter referred to as the DG method, is well suited for advection-dominated problem and leads to algorithms scaling very well on a large number of processors. They also facilitate the computation of explicit time methods and can easily be extended to higher order of accuracy in a natural way. On a given mesh, a DG method offers a higher precision than a classical finite element method with the same formal order of accuracy but requires significantly more discrete unknowns as well as the computation of additional terms at the boundaries between elements.

Since diffusion is very low in the deep ocean basins and water masses can remain unchanged for years, spurious mixing is a crucial issue in global circulation models (MacCready et al., 2018). This mixing constitutes a problem even for coastal domains that are characterised by strong horizontal and vertical density gradients (Geyer and MacCready, 2014; MacCready and Geyer, 2010), small scale dynamics as internal waves and baroclinic eddies. As a result, an overly diffusive model cannot capture essential features like the intrusion of saline waters into embayments or the mixing in river plumes Burchard and Rennau (2008); Hofmeister et al. (2010); Kärnä et al. (2015); Ralston et al. (2017). The finite grid resolution and the numerical schemes, in particular the discretization of the advection, can introduce significant spurious numerical mixing (Burchard and Rennau, 2008; Rennau and Burchard, 2009; Hiester et al., 2014).

To fully discretize the hydrodynamic equations, time integration methods are required. Splitting techniques are widely used e.g. Wicker and Skamarock (2002); Knoth and Wensch (2003); Nilsen and Loseth (1993); Visbal and Gaitonde (2002); Robert and Kaper (1986). The fast surface gravity waves propagating in a depth integrated 2D framework are coupled to the slower 3D dynamics. In a split-explicit scheme (SPEX), the 2D mode is solved explicitly with a small time step while the 3D one uses a larger time step (Gadd, 1978, 1980; Killworth et al., 1991; Shchepetkin A.F., 2005). Fast waves limit the time step. For long simulations, which are not uncommon in the marine domain, this can lead to a large number of time steps. This leans on computational and storage resources. In split-implicit schemes, the 2D and 3D modes generally use the same time-step but an implicit method is used for the 2D while the 3D is solved explicitely, e.g. Dukowicz and Smith (1994); Marshall et al. (1997). Those schemes tend to be expensive for ocean models where the resolution of the nonlinear partial differential equations requires iterative methods.

The Second-generation Louvain-la-Neuve Ice-ocean Model (SLIM, www.slim-ocean.be) focuses on solving the hydrodynamic equations on an unstructured grid. As ocean and coastal domain can feature strong scalar field and velocity gradients, it is important to maintain a good quality of these fields. One drawback of many unstructured grid models is their excessive numerical diffusion that smooths out important physical features (Kärnä et al., 2015; Kärnä and Baptista, 2016; Comblen et al., 2010).

To address this issue, this work presents a new second order split-explicit Runge-Kutta (SPEX-RK) temporal scheme combined with the DG spatial discretization of SLIM. The objective is specifically to obtain a low numerical mixing, a second-order accurate, conservative and consistent tracer advection scheme. This requires a fully discontinuous treatment of the free surface motion in order to achieve conservation of water and tracer volumes both locally and globally. All horizontal terms are processed by an explicit method. Only the vertical terms are treated implicitly. This choice guarantees an easy and efficient parallelization of the model, as the evolution of each vertical column over a time step can be computed independently.

This article is organised as follows. It starts by introducing the split-explicit Runge-Kutta time integrators in Section 2. In the next section, the hydrodynamic equations, their DG-FE discretisation, the integration of the temporal scheme in our marine model and the methods to ensure conservation and consistency are presented. In Section 4, various numerical results on different test cases are shown to validate our model. Finally, a conclusion is given at the end of this article in Section 5.

2. Split-Explicit Runge-Kutta methods

First of all, it is worth recalling the notion of stiffness of a problem. Let us consider an initial value problem associated with two different processes: a slow process and a fast one. Each process has its own characteristic timescale. When the magnitudes of the timescales are significantly different, the system is said to be stiff.

2.1. Temporal scheme

In practice, for an initial value problem with many processes, if the maximum value of the time step is mainly limited by a single term representing one process, the problem is said to be stiff. For illustration purposes, the following ordinary differential equation is taken into consideration:

$$\frac{\mathrm{d}y}{\mathrm{d}t} = f(y) + F(y), \quad t \in (0, T) \tag{1}$$

with the initial value $y(0) = y_0$.

The functions $f(y)$ and $F(y)$ correspond to the non-stiff (slow time-varying) and the stiff (fast time-varying) parts, respectively. Note that they could be the result of applying two different spatial discretizations for the two differential operators associated with slow and fast processes. To solve this type of equation, a splitting methods can be used. For example, Runge-Kutta (RK) methods can be used with a big time step, Δt, for the temporal evolution of $f(y)$ and a small one, $\Delta T = \frac{\Delta t}{M}$ with M the closest suitable integer to the ratio between the characteristic timescales, for the temporal evolution of $F(y)$.

The main objective of this article is to obtain a second order temporal scheme. For this purpose, as pointed out in Knoth and Wensch (2013), one can use a Runge-Kutta of order 2 with 3 steps (RK3) for slow terms and a Runge-Kutta of order 2 with 2 steps (RK2) for the fast ones to ensure it. The combination of these two temporal scheme gives the SPEX-RK scheme. The RK3 is used to have a bigger stability region. For the random variables y_n and Y_n, respectively, the two chosen schemes are the following ones

$$\begin{aligned} y_{n+1} &= y_n + \Delta t k_3 \\ k_1 &= f(t_n, y_n) \\ k_2 &= f(t_n + \Delta t/3, y_n + k_1 \Delta t/3) \\ k_3 &= f(t_n + \Delta t/2, y_n + k_2 \Delta t/2) \end{aligned} \qquad \begin{aligned} Y_{n+1} &= Y_n + \Delta T K_2 \\ K_1 &= F(t_n, Y_n) \\ K_2 &= F(t_n + \Delta T/2, Y_n + K_1 \Delta T/2) \end{aligned}$$

These RK are low-storage temporal schemes, meaning that for each evaluation of the solution, one just needs to keep few data in memory.

Let us describe the original SPEX-RK for Equation 1. Firstly, k_1^{slow} is computed using y_0 such that $k_1^{\text{slow}} = f(y_0)$. This allows the slow terms to reach $y_{n+\frac{1}{3}}$. A loop from 1 to $\frac{M}{3}$ moves the fast terms using RK2 to $Y_{n+\frac{1}{3}}$ by calculating k_1^{fast} and k_2^{fast} at each iteration. $Y_{n+\frac{1}{3}}$ and $y_{n+\frac{1}{3}}$ are added to obtain the total value of the variable. Afterwards, the same process is repeated with k_2^{slow} and k_3^{slow}. Finally, y_{n+1} is found by using k_3^{slow}. The whole process is summarised in the Figure 1 and the Algorithm 1. Although this temporal scheme uses two well-known RK, the resulting splitting is new.

2.2. Order of precision

While the Knoth and Wensch (2013) suggests that this scheme has a second order accuracy, it still needs to be verified through analysis. To achieve this, the Taylor series expansion of y_{n+1} must match the result of the temporal scheme up to order 2. The former can be expressed as:

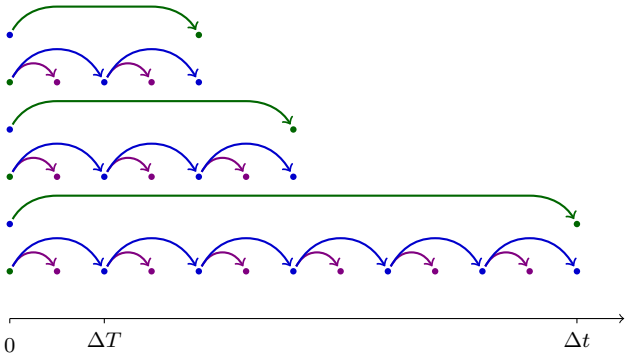

Figure 1: Split-explicit scheme composed by RK3 and RK2. The green arrows represent the computation of each $f^{\text{slow}}(y)$ while the blue and the purple ones represent the computation of each $f^{\text{fast}}(y)$

Algorithm 1: SPEX-RK scheme for RK3 and RK2

Data: Model state variable y_n, $m = M/6$

$y_0 \leftarrow y_n$
$y \leftarrow y_n$
for $i = 2m, 3m, 6m$ **do**
  $k^{\text{slow}} \leftarrow f^{\text{slow}}(y)$
  $y \leftarrow y_0$
  for $j = 1, \ldots, i$ **do**
    $k^{\text{fast}} \leftarrow f^{\text{fast}}(y)$
    $k^{\text{fast}} \leftarrow f^{\text{fast}}(y + \frac{1}{2}\Delta T(k^{\text{fast}} + k^{\text{slow}}))$
    $y \leftarrow y + \Delta T(k^{\text{fast}} + k^{\text{slow}})$
$y_{n+1} \leftarrow y$

$$
\begin{aligned}
y_{n+1} &= y_n + \Delta t y_n^{'} + \frac{\Delta t^2}{2} y_n^{''} + O(\Delta t^3) \\
&= y_n + \Delta t \left(f_n + F_n\right) + \frac{\Delta t^2}{2}\left(\left(f_n^{'} + F_n^{'}\right)\left(f_n + F_n\right)\right) + O(\Delta t^3)
\end{aligned} \tag{2}
$$

with $f_n = f(y_n)$ and $F_n = F(y_n)$.

A classic Runge-Kutta order analysis would compute each iteration of the residues and sum them up to obtain the final expression of y_{n+1}. For a SPEX-RK scheme, this is not practical to show the result of each 2D sub-steps, which involves too many terms to express. Instead, for clarity, only the evaluations of y at the 3D sub-steps are computed, which include $y_{n+\frac{1}{3}}, y_{n+\frac{1}{2}}$, and y_{n+1}. The complete development can be found in Appendix A. Following Algorithm 1, the first sub-steps gives:

$$
y_{n+\frac{1}{3}} = y_n + \frac{\Delta t}{3}\left(f_n + F_n\right) + \frac{1}{9}\frac{\Delta t^2}{2}\left(F_n^{'}\left(f_n + F_n\right)\right) + O(\Delta t^3) \tag{3}
$$

Using this result, the second sub-step can be obtained.

$$
y_{n+\frac{1}{2}} = y_n + \frac{\Delta t}{2}\left(f_n + F_n\right) + \frac{1}{4}\frac{\Delta t^2}{2}\left(\left(\frac{4}{3}f_n^{'} + F_n^{'}\right)\left(f_n + F_n\right)\right) + O(\Delta t^3) \tag{4}
$$

The final sub-step gives

$$
y_{n+1} = y_n + \Delta t \left(f_n + F_n\right) + \frac{\Delta t^2}{2}\left(\left(f_n^{'} + F_n^{'}\right)\left(f_n + F_n\right)\right) + O(\Delta T^3) \tag{5}
$$

Comparing the two equations, it can be concluded that Equation 2 matches Equation 5. Therefore, the SPEX-RK scheme is a temporal scheme of order 3 locally and order 2 globally.

2.3. Stability Region

In order to obtain the stability condition of a numerical method, it is common practice to analyze the linear version of the underlying ordinary differential equation. In the case of the method under consideration, we have the following linear ODE:

$$
\frac{\mathrm{d}y}{\mathrm{d}t} = \lambda y + \Lambda y \tag{6}
$$

Here, λ and Λ respectively denote the complex coefficients of the linear functions $f(y)$ and $F(y)$.

The amplification factor of the numerical solution at each time step is defined as the ratio between y_{n+1} and y_n. Using Algorithm 1, this factor can be expressed as:

$$
\begin{aligned}
\frac{y_{n+1}}{y_n} = A^M &+ \lambda A^{\frac{M}{2}}\left(\Delta T + \Lambda\frac{\Delta T^2}{2}\right)\left(\frac{1-A^M}{1-A}\right) + \lambda^2 A^{\frac{M}{3}}\left(\Delta T + \Lambda\frac{\Delta T^2}{2}\right)^2\left(\frac{1-A^{\frac{M}{2}}}{1-A}\right)\left(\frac{1-A^M}{1-A}\right) \\
&+ \lambda^3\left(\Delta T + \Lambda\frac{\Delta T^2}{2}\right)^3\left(\frac{1-A^{\frac{M}{3}}}{1-A}\right)\left(\frac{1-A^{\frac{M}{2}}}{1-A}\right)\left(\frac{1-A^M}{1-A}\right)
\end{aligned} \tag{7}
$$

with $A = \left(\frac{\Lambda^2 dT^2}{2} + \Lambda dT + 1\right)$ and $\Delta t = M\Delta T$. All the details are in Appendix B.

The stability of the scheme depends on whether the norm of the amplification factor is less than or equal to 1. The stability region of the scheme is a function of three parameters: λ, Λ, and M, where the first two

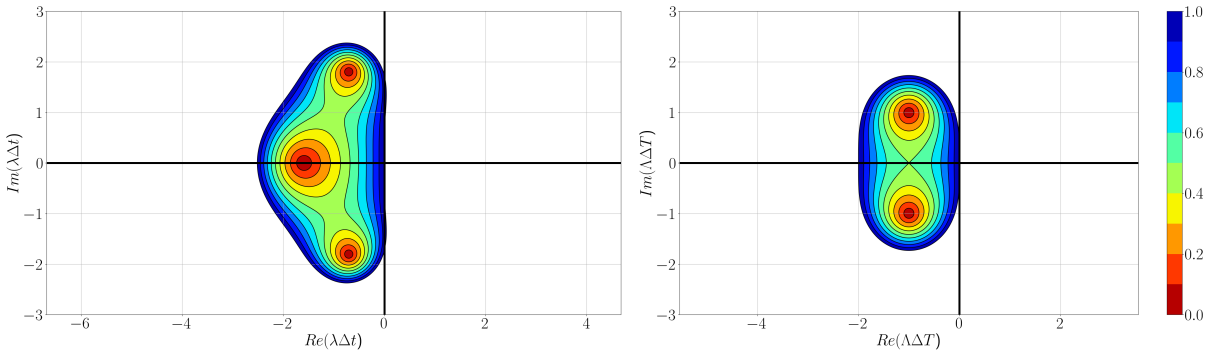

Figure 2: Stability region with only one function with M = 1. The abscissa is the Real part while the ordinates is the Imaginary part of respectively $\lambda\Delta t$ and $\Lambda\Delta T$. The bold lines are the origins.

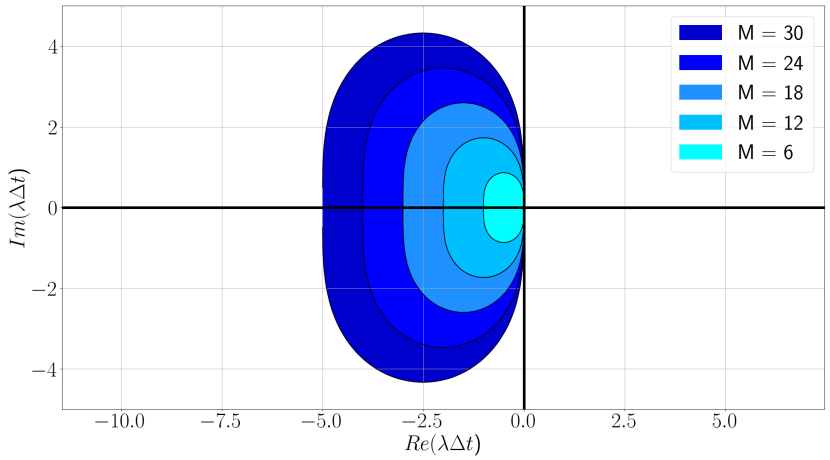

Figure 3: Stability region with $\lambda = 1$ and $\Lambda = 12$ and $M = [6, 12, 18, 24, 30]$ while Δt stays the same. The abscissa is the Real part while the ordinates is the Imaginary part of $\lambda\Delta t$. The bold lines are the origins.

are complex and the last is a positive integer. The global stability region is too complicated to represent, as it is a 5D field. To facilitate the representation of the function, let us consider first the case where λ or Λ is null and $M = 1$. Figure 2 shows the corresponding stability regions, which match those of the classic RK3 and RK2 methods. Increasing the value of M affects both graphs: for RK3, the stability region is reduced but maintains the same shape, while for RK2, the region remains the same size but the area with a small amplification factor increases.

The focus is on the case where Λ is bigger than λ. For simplicity, a specific case is being considered that can be generalized. The magnitudes of $|\Lambda|$ and $|\lambda|$ are respectively 12 and 1, and M increases while ΔT decreases such that $M\Delta T$ remains constant. The factor M takes the value from the set [6, 12, 18, 24, 30]. The first entry in the set considers a factor smaller than the ratio between the eigenvalues of the fast and slow process. The second entry considers a factor equal to the ratio, while the last values are greater than the latter. The stability regions are shown in Figure 3.

Each stability region has the shape of the classic RK2. When M is equal to the ratio, the region has the same size as the RK2. For a smaller M, the region is reduced, while for a larger M, the region is increased. This implies that when Δt is larger, M must be increased as well.

3. Model

The presented scheme is applied to the ocean. This study focuses on the three-dimensional hydrostatic equations with a focus on two ranges of timescales. The scale-separation stiffness can be described by the external Froude number. This dimensionless number characterises the ratio between the water velocity and the gravity wave speed.

3.1. Governing equations

The studied equations are derived from the Navier-Stokes equations under the hydrostatic hypothesis with the Boussinesq approximation. The first assumption means that the pressure force balances the weight of the water column. The Boussinesq approximation implies that density variations are neglected in all terms of the momentum equation, except the gravity term. Given the Cartesian horizontal and vertical coordinates $\mathbf{x} = [x, y, z]^T$, they take the following form

$$\frac{\partial \mathbf{u}}{\partial t} + \boldsymbol{\nabla}_h \cdot (\mathbf{u}\mathbf{u}) + \frac{\partial (w\mathbf{u})}{\partial z} = \boldsymbol{\nabla}_h \cdot (\nu_h \boldsymbol{\nabla}_h \mathbf{u}) + \frac{\partial}{\partial z}\left(\nu_v \frac{\partial \mathbf{u}}{\partial z}\right) \tag{8a}$$

$$- f\mathbf{e}_z \times \mathbf{u} - g\boldsymbol{\nabla}_h \eta - \frac{g}{\rho_0}\mathbf{q} - \frac{g}{\rho_0}\rho'|_\eta \boldsymbol{\nabla}_h \eta$$

$$\frac{\partial H}{\partial t} = -\boldsymbol{\nabla}_h \cdot \int_{-b}^{\eta} \mathbf{u} dz \tag{8b}$$

$$\frac{\partial w}{\partial z} = -\boldsymbol{\nabla}_h \cdot \mathbf{u} \tag{8c}$$

where ν_h, ν_v and $\boldsymbol{\nabla}_h$ respectively represent the horizontal as well as the vertical viscosity and the horizontal gradient. $\mathbf{u} = (u,v)$ is the horizontal velocity vector while w is the vertical velocity. The horizontal total transport is represented by the variables $\mathbf{U} = \int_{-b}^{\eta} \mathbf{u} dz$ with η and b respectively the free surface elevation and the bathymetry. The height of the column is represented by H . f is the Coriolis parameter. $\mathbf{q}$ represents the integral of the density deviation gradient, $\mathbf{q} = \int_{-b}^{\eta} \boldsymbol{\nabla}_h \rho'$. The density deviation is obtained by a state equation depending on the water temperature or the salinity.

Water temperature and salinity are modeled by the advection-diffusion equation. This gives

$$\rho' = \rho'(T, S) \tag{9}$$

$$\frac{\partial T}{\partial t} + \boldsymbol{\nabla}_h \cdot (\mathbf{u}T) + \frac{\partial (wT)}{\partial z} = \boldsymbol{\nabla}_h \cdot (\kappa_h \boldsymbol{\nabla}_h T) + \frac{\partial}{\partial z}\left(\kappa_v \frac{\partial T}{\partial z}\right) \tag{10}$$

$$\frac{\partial S}{\partial t} + \boldsymbol{\nabla}_h \cdot (\mathbf{u}S) + \frac{\partial (wS)}{\partial z} = \boldsymbol{\nabla}_h \cdot (\kappa_h \boldsymbol{\nabla}_h S) + \frac{\partial}{\partial z}\left(\kappa_v \frac{\partial S}{\partial z}\right) \tag{11}$$

κ_h and κ_v stand for respectively the horizontal and the vertical diffusivity.

Furthermore, SLIM solves the equations in a three-dimensional domain Ω with a free moving surface. The lateral boundary Γ_l is fixed as well as the bottom boundary Γ_b. However, the surface boundary Γ_s varies in time with the vertical coordinates between the $z = -b$ and $z = \eta$. The impermeability conditions are prescribed on the top and the bottom surfaces:

$$w + \mathbf{u} \cdot \boldsymbol{\nabla}_h b = 0 \qquad \mathbf{x} \in \Gamma_b \tag{12a}$$

$$w - \frac{\partial H}{\partial t} - \mathbf{u} \cdot \boldsymbol{\nabla}_h (H - b) = 0 \qquad \mathbf{x} \in \Gamma_s \tag{12b}$$

In addition, a slip condition is applied to account for bottom and surface stresses, $\boldsymbol{\tau}_b$ and $\boldsymbol{\tau}_s$,

$$\nu_v \frac{\partial \mathbf{u}}{\partial z} = \frac{\boldsymbol{\tau}_b}{\rho_0} \qquad \mathbf{x} \in \Gamma_b \tag{13a}$$

$$\nu_v \frac{\partial \mathbf{u}}{\partial z} = \frac{\boldsymbol{\tau}_s}{\rho_0} \qquad \mathbf{x} \in \Gamma_s \tag{13b}$$

$$\tag{13c}$$

3.2. Weak formulation

To obtain the weak formulation, the previous continuous equations have to be multiplied by a smooth 2D shape function $\phi_i(x, y)$ or 3D shape function $\phi_i(x, y, z) = \phi_{j,xy}(x, y)\ \phi_{k,z}(z)$ with j and k the indexes for respectively the horizontal and vertical discontinuous nodes. These equations are discretised with a discontinuous linear function space. They are then integrated by part to obtain volume terms and interface terms. The interface terms can be integrals on a horizontal triangle domain or a vertical squad domain.

In the weak form, the following notations are used for the volume and the interface integrals

$$\left\langle \bullet \right\rangle = \int_\Omega \bullet \mathrm{d}V$$

$$\left\langle\left\langle \bullet \right\rangle\right\rangle_{\partial\Gamma_h} = \int_{\partial\Gamma_h} \bullet \mathrm{d}S$$

$$\left\langle\left\langle \bullet \right\rangle\right\rangle_{\partial\Gamma_v} = \int_{\partial\Gamma_v} \bullet \mathrm{d}S$$

Ω represents the domain while $\partial\Gamma$ represents the interfaces. In 3D, they can be vertical faces, Γ_v, or horizontal faces, Γ_h. In 2D, all the interfaces are edges.

The equation for $\mathbf{u}$ has 3D and 2D terms. The latter, corresponding to the fast processes, are split such that there are two types of functions spaces, 2D and 3D. In the interfaces integrals, a mean value is used for the terms with the horizontal velocities. It is computed such that

$$\{\mathbf{u} \cdot \mathbf{n}_h\} = \frac{\mathbf{u}_{right} \cdot \mathbf{n}_h + \mathbf{u}_{left} \cdot \mathbf{n}_h}{2} \tag{14a}$$

$$\{w\} = \frac{w_{right} + w_{left}}{2} \tag{14b}$$

where $\{\cdot\}$ represents the mean operator between values on both sides of the interfaces. The same reasoning is used for the terms with the vertical velocity. What's more, in the vertical interfaces integrals, an upwind term is used, $\mathbf{u}^{up}$ in addition to the terms described before. Equation 8a becomes

$$\left\langle \phi_i \frac{\partial \mathbf{u}}{\partial t} \right\rangle = f_{3d}(\mathbf{u}) + \frac{1}{H} f_{2d}(H\mathbf{u}) \tag{15a}$$

with

$$
\begin{aligned}
f_{2d}(H\mathbf{u}) &= \left\langle g\left(1+\frac{\rho'|_\eta}{\rho_0}\right)\frac{H^2}{2}\boldsymbol{\nabla}_h\cdot\boldsymbol{\phi}_i\right\rangle - \left\langle\left\langle g\left(1+\frac{\rho'|_\eta}{\rho_0}\right)\frac{H^{*2}}{2}\boldsymbol{\phi}_i\cdot\mathbf{n}\right\rangle\right\rangle \\
&+ \left\langle\phi_i g\left(1+\frac{\rho'|_\eta}{\rho_0}\right)H\boldsymbol{\nabla}_h b\right\rangle + \left\langle\frac{g}{\rho_0}\frac{H^2}{2}\boldsymbol{\nabla}_h\left(\rho'|_\eta\right)\phi_i\right\rangle \\
&= \left\langle g\left(1+\frac{\rho'|_\eta}{\rho_0}\right)\frac{H^2}{2}\boldsymbol{\nabla}_h\cdot\boldsymbol{\phi}_i\right\rangle - \left\langle\left\langle g\left(1+\frac{\rho'|_\eta}{\rho_0}\right)\left(\frac{H_{left}^2+H_{right}^2}{4}\right)\boldsymbol{\phi}_i\cdot\mathbf{n}\right\rangle\right\rangle \\
&+ \left\langle\phi_i g(1+\frac{\rho'|_\eta}{\rho_0})H\boldsymbol{\nabla}_h b\right\rangle + \left\langle\frac{g}{\rho_0}\frac{H^2}{2}\boldsymbol{\nabla}_h\left(\rho'|_\eta\right)\phi_i\right\rangle \\
f_{3d}(\mathbf{u}) &= \left\langle\mathbf{u}\mathbf{u}\cdot\boldsymbol{\nabla}_h\phi_i\right\rangle - \left\langle\left\langle\phi_i\mathbf{u}^{up}\left\{\mathbf{u}\cdot\mathbf{n}_h\right\}\right\rangle\right\rangle_{\Gamma_h\cup\Gamma_v} + \left\langle w\mathbf{u}\frac{\partial\phi_i}{\partial z}\right\rangle \\
&- \left\langle\left\langle\phi_i\left\{w\right\}\mathbf{u}^{up}n_z\right\rangle\right\rangle_{\Gamma_h} - \left\langle\phi_i\mathbf{f}\times\mathbf{u}\right\rangle - \left\langle\phi_i\mathbf{q}\right\rangle + \text{Diffusion}
\end{aligned}
$$

The diffusive terms have not been developed for more clarity.

With $i = 1, ..., n$, with n being the number of discontinuous nodes, the vertical velocity equation becomes

$$
-\left\langle\frac{\partial\phi_i}{\partial z}w\right\rangle + \left\langle\left\langle\phi_i\left\{w\right\}n_z\right\rangle\right\rangle_{\Gamma_h} = \left\langle\mathbf{u}\cdot\boldsymbol{\nabla}_h\phi_i\right\rangle - \left\langle\left\langle\phi_i\left\{\mathbf{u}\cdot\mathbf{n}_h\right\}\right\rangle\right\rangle_{\Gamma_h\cup\Gamma_v} \tag{16}
$$

The weak formulation of the temperature, the salinity or a scalar field equation is derived analogously. For more clarity, the development are shown only for the temperature equation.

$$
\begin{aligned}
\left\langle\phi_i\frac{\partial T}{\partial t}\right\rangle &= \left\langle\mathbf{u}T\cdot\boldsymbol{\nabla}_h\phi_i\right\rangle - \left\langle\left\langle\phi_i T^{up}\left\{\mathbf{u}\cdot\mathbf{n}_h\right\}\right\rangle\right\rangle_{\Gamma_h\cup\Gamma_v} \\
&+ \left\langle wT\frac{\partial\phi_i}{\partial z}\right\rangle - \left\langle\left\langle\phi_i\left\{w\right\}T^{up}n_z\right\rangle\right\rangle_{\Gamma_h} + \text{Diffusion}
\end{aligned} \tag{17}
$$

Unlike the previous horizontal velocities, H is a 2D variables. Therefore, the function space is 2D. In the interface integrals, stabilisation terms are added by means of the Lax-Friedrichs approximated solver. With $i = 1, ..., n$, it gives

$$
\left\langle\phi_i\frac{\partial H}{\partial t}\right\rangle = \left\langle\mathbf{U}\cdot\boldsymbol{\nabla}_h\phi_i\right\rangle - \left\langle\left\langle\phi_i\mathbf{U}^*\cdot\mathbf{n}_h\right\rangle\right\rangle \tag{18a}
$$

with

$$
\begin{aligned}
\mathbf{U}^* &= \frac{(\mathbf{U}_{left}+\mathbf{U}_{right})\cdot\mathbf{n}_h}{2} - c\frac{(H_{left}-h_{left})-(H_{right}-h_{right})}{2} \\
c &= \max\left(\sqrt{gH_{left}}+\left|\left|\frac{\mathbf{U}_{n,left}}{H_{left}}\right|\right|, \sqrt{gH_{right}}+\left|\left|\frac{\mathbf{U}_{n,right}}{H_{right}}\right|\right|\right)
\end{aligned}
$$

3.3. 3D and 2D link

In the weak form of the all previous equations, the integrals are made on the elements of the mesh. Three-dimensional volume terms are integrated on prisms, Ω, while the two-dimensional ones on triangles, Ω_{2D}. The 3D interfaces terms are either integrated on horizontal triangles, Γ_h, or vertical squads, Γ_h, while

2D ones on edges, Γ_{2D}. For ease of computation, all theses integrals are done on parent elements denoted by $\hat{\Omega}$ or $\hat{\Gamma}$. The parent triangle is the unit triangle of area 0.5 while the parent vertical and horizontal edge are segments of length 2. These spatial transformations introduce new coefficients : A the area of the 2D horizontal extruded triangles, $h = h(x, y)$ the vertical height of each prisms and l the length of the edges of the mentioned triangles. By taking $h\mathbf{u}$ as the advection field instead of $\mathbf{u}$ for the vertical velocity in the weak form, it can be shown that the vertical integrals of the 3D terms become the terms with 2D velocity by using numerical integrals. The vertical sum of the 3D volume terms becomes

$$\begin{aligned}
\sum_z \left\langle h\mathbf{u}\cdot\boldsymbol{\nabla}_h\phi_i \right\rangle_\Omega &= \sum_z \left\langle 2A\left(\frac{h}{2}\mathbf{u}\right)\cdot\boldsymbol{\nabla}_h\phi_i \right\rangle_{\hat{\Omega}} \\
&= \sum_z\sum_p \left(2A\left(\sum_q \left(\frac{h}{2}\mathbf{u}\right)_q \phi_{q,xy}\phi_{q,z}\right)\cdot\boldsymbol{\nabla}_h\phi_i\right)_{\hat{\Omega},p} \\
&= \sum_p \left(2A\left(\sum_q (H\bar{\mathbf{u}})_q\,\phi_{q,xy}\right)\cdot\boldsymbol{\nabla}_h\phi_{i,xy}\right)_{\hat{\Omega}_{2D},p} \\
&= \left\langle 2A\,(H\bar{\mathbf{u}})\cdot\boldsymbol{\nabla}\phi_{i,xy}\right\rangle_{\hat{\Omega}_{2D}} \\
&= \left\langle \mathbf{U}\cdot\boldsymbol{\nabla}\phi_{i,xy}\right\rangle_{\Omega_{2D}}
\end{aligned}$$

The vertical sum of the 3D vertical squad interface terms becomes

$$\begin{aligned}
\sum_z \left\langle\left\langle \{h\mathbf{u}\cdot\mathbf{n}_h\}\,\phi_i\right\rangle\right\rangle_{\Gamma_v} &= \sum_z \left\langle\left\langle \frac{l}{2}\left\{\frac{h}{2}\mathbf{u}\cdot\mathbf{n}_h\right\}\phi_i\right\rangle\right\rangle_{\hat{\Gamma}_v} \\
&= \sum_z\sum_p \left(\frac{l}{2}\left\{\sum_q ((H\bar{\mathbf{u}})_q\phi_{q,xy}\phi_{q,z})\cdot\mathbf{n}_h\right\}\phi_i\right)_{\hat{\Gamma}_{2D,v}} \\
&= \sum_p \left(\frac{l}{2}\left\{\sum_q ((H\bar{\mathbf{u}})_q\phi_{q,xy})\cdot\mathbf{n}_h\right\}\phi_{i,xy}\right)_{\hat{\Gamma}_{2D,v}} \\
&= \left\langle\left\langle \frac{l}{2}\{H\bar{\mathbf{u}}\cdot\mathbf{n}_h\}\,\phi_{i,xy}\right\rangle\right\rangle_{\hat{\Gamma}_{2D,v}} \\
&= \left\langle\left\langle \{\mathbf{U}\cdot\mathbf{n}_h\}\,\phi_{i,xy}\right\rangle\right\rangle_{\Gamma_{2D,v}}
\end{aligned}$$

In the interface integrals, 3D stabilisation terms are added to match the Riemann solvers in the 2D equation.

3.4. Temporal integration and ALE formulation

For the temporal scheme, a split explicit second order Runge-Kutta method is used. It consists of a RK3 for the 3D part of the velocity equation and a RK2 for the 2D one. The two temporal schemes are those describes in Section 2 with time steps Δt and ΔT respectively. The ratio, M, between the two time steps is the closest integer to the ratio of the highest propagation speed in the external mode to the highest speed of the external gravity waves. The variables y corresponds the horizontal velocity $\mathbf{u}$, the vertical coordinates represented by the vertical height of each prisms h, the temperature T and the salinity S while Y corresponds to horizontal total transport $\mathbf{U}$ and the water height H. All the other variables $\mathbf{w}$, $\mathbf{q}$, ρ' and η, can be obtained at any time from these primary variables. The finite element method introduces mass matrices. M^n is the global mass matrix at the time n. Therefore, to apply these two temporal schemes to

our problem, one must take into account the change of the mass matrix through time in the algorithm. An arbitraty Lagrangian-Eulerian scheme is introduced to take into account the vertical displacement of the mesh. As the three-dimensional mesh follows the movement of the free surface, only the vertical coordinates move with time (e.g. (Clare et al., 2022; Pan et al., 2019)).

A complete iteration of the three-dimensional hydrostatic equations is shown in Algorithm 2. First, $\mathbf{u}$ and h are used to obtain the 2D variables, $\mathbf{U}$ and H, at the beginning of the time step. Each external mode sub-iteration are done following the same process. For each sub-time step i, the horizontal terms of the three-dimensional discretized velocity equations, $\mathbf{f}^{\text{hor}}$, is obtained. The friction terms are also computed in this term. This 3D residue is integrated over the water columns to obtained the 2D term $\mathbf{F}^{\text{hor}}$. The vertical terms without the friction terms can be omitted because their vertical integrals are zero. The two-dimensional variables are moved to the right sub-time using $\mathbf{F}^{\text{hor}}$. Throughout the iterations, the sum of all the residues of the 2D velocity equation multiplied by the small time step, $\mathbf{F}^{\text{fast}} = \sum_{j=1}^{i} \Delta T \mathbf{F}_{\mathbf{U}}$, is obtained. The new vertical height is known at the end of the internal sub-iteration. Therefore, the position of the mesh can be updated. Finally, the horizontal velocity is obtained by computing the vertical terms of three-dimensional velocity equations, $\mathbf{f}^{\text{ver}}$, taking into consideration the horizontal and the 2D terms.

$$M_{3d}\mathbf{u} - M_{3d}^{0}\mathbf{u}^{0} = \frac{i\Delta t}{M}(\mathbf{f}^{\text{hor}} + \mathbf{f}^{\text{ver}}) + \frac{1}{2}\frac{h}{H}\mathbf{F}^{\text{fast}}$$

Algorithm 2: SPEX-RK iteration for the hydrodynamic equations, $m = M/6$

Data: Model state variable $\mathbf{u}, z$
$\mathbf{U}, H \leftarrow \sum_z \frac{h}{2}\mathbf{u}, \sum_z \frac{h}{2}$
$\mathbf{u}_0, h_0 \leftarrow \mathbf{u}, h$
$\mathbf{U}_0, H_0 \leftarrow \mathbf{U}, H$
for *i=2m, 3m, 6m* **do**
  $\mathbf{f}^{\text{hor}} \leftarrow f_{3d}^{\text{hor}}(\mathbf{u}, z)$
  $\mathbf{F}^{\text{hor}} \leftarrow \sum_z \mathbf{f}^{\text{hor}}$
  $\mathbf{U}, H \leftarrow \mathbf{U}_0, H_0$
  $\mathbf{F}^{\text{fast}} \leftarrow 0$
  for *j=1,...,i* **do**
    $\mathbf{F}_{\mathbf{U}}, F_H \leftarrow F_{2d}(\mathbf{U}, H)$
    $\mathbf{F}_{\mathbf{U}}, F_H \leftarrow F_{2d}(\mathbf{U} + \frac{\Delta T}{2} M_{2d}^{-1}(\mathbf{F}_{\mathbf{U}} + \mathbf{F}^{\text{hor}}), H + \frac{\Delta T}{2} M_{2d}^{-1} F_H)$
    $\mathbf{U} \leftarrow \mathbf{U} + \Delta T M_{2d}^{-1}(\mathbf{F}_{\mathbf{U}} + \mathbf{F}^{\text{hor}})$
    $H \leftarrow H + \Delta T M_{2d}^{-1} F_H$
    $\mathbf{F}^{\text{fast}} \leftarrow \mathbf{F}^{\text{fast}} + \Delta T \mathbf{F}_{\mathbf{U}}$
  Update the z coordinates based on H
  $\mathbf{u} \leftarrow M_{3d}^{-1}\left(M_{3d}^{0}\mathbf{u}_0 + \frac{i\Delta t}{M}\left(\mathbf{f}^{\text{hor}} + \mathbf{f}^{\text{ver}}\right) + \frac{1}{2}\frac{h}{H}\mathbf{F}^{\text{fast}}\right)$

3.5. Conservation and Consistency

In order to be coherent with the basic physics of hydrodynamic flows, the temporal scheme and the spatial discritisations must respect two main properties. The first one concerns tracer concentration through the domain and the second one the conservation of the amount of water and tracer. The general idea behind tracer consistency is that if the tracer concentration is uniform over the domain, then it should remain uniform at all time. The conservation states that the volume of water and tracer must remain constant in a domain isolated from its environment. To respect simultaneity the tracer conservation and consistency, the temporal scheme as well as the discretisation of the method has to be chosen in a proper way. White et al. (2007) explains it for a different scheme.

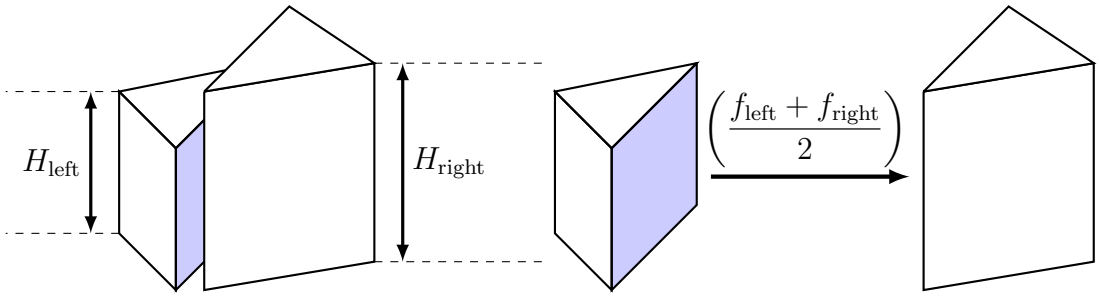

Figure 4: Flux between two prisms in a discontinued mesh with 1 layer

3.5.1. Water conservation

All the discretised variables in the presented equations are discontinuous. The hydrodynamic velocities, the tracer concentration and especially the elevation have multiple values for the same points. The latter leads to a discontinuous mesh. Two adjacent prisms have slightly discontinuous vertical coordinates. To ensure the water and tracer conservation, the focus is put on the fluxes (Berger and Howington, 2002). Unique fluxes are computed as the mean between the flux evaluated on the left and right prisms (see Figure 4).

The fluxes problems fixed, the water conservation still has to be demonstrated. The water height Equation 18a is analysed in a closed domain. The equation is summed up for each $i \in [0, m]$, m being the number of discontinuous nodes.

$$\sum_{i=1}^{m} \left\langle \phi_i \frac{\partial H}{\partial t} \right\rangle = \sum_{i=1}^{m} \left\langle \mathbf{U} \cdot \boldsymbol{\nabla}_h \phi_i \right\rangle \tag{19}$$

$$+ \sum_{i=1}^{m} \left\langle \left\langle \phi_i \left(\frac{\mathbf{U}_{n,left} + \mathbf{U}_{n,right}}{2} - c \frac{H_{left} + H_{right}}{2} \right) \right\rangle \right\rangle \tag{20}$$

The sum and the integrals permute. By remembering that by definition the sum of ϕ_i and $\boldsymbol{\nabla}\phi_i$ equals respectively to 1 and 0, the previous equation becomes

$$\left\langle \frac{\partial H}{\partial t} \right\rangle = \left\langle \left\langle \left(\frac{\mathbf{U}_{n,left} + \mathbf{U}_{n,right}}{2} - c \frac{H_{left} + H_{right}}{2} \right) \right\rangle \right\rangle \tag{21}$$

For each edge that is not at the boundary of the domain, the flux receives by the left element is the same as the flux gives by the right one. The normal vector of the two prisms are opposite. The sum of all the fluxes inside the domain is 0. At the boundaries, all the fluxes are zero because the domain is closed. The equation finally becomes

$$\left\langle \frac{\partial H}{\partial t} \right\rangle = 0 \tag{22}$$

This proves the water conservation.

3.5.2. Surface impermeability

In this section, the demonstration is done for one big time step using Δt but it stays valid for each sub-time step. To numerically ensure the conservation and the consistency of the tracer, the surface impermeability condition of continuity Equation 16 must be respected as stated in (Deleersnijder, 1993; Campin et al.,

2004; Deleersnijder and Campin, 1995). To achieve that, the following equation is used to compute the mesh velocity w_m. For each $i \in [0, m]$, m being the number of discontinuous nodes, it gives

$$\frac{\left\langle \phi_i \right\rangle^{n+1} - \left\langle \phi_i \right\rangle^{n}}{\Delta t} = -\left\langle w_m \frac{\partial \phi_i}{\partial z} \right\rangle^{n} + \left\langle \left\langle w_m^d \phi_i n_z \right\rangle \right\rangle_{\Gamma_h}^{n} \tag{23}$$

By summing only the vertical part of the ϕ_i, this equation can be simplified. The left-hand side (LHS) equals the integral of the difference of the water height between two 3D time step. In the right-hand side (RHS), only the fluxes through the horizontal interfaces remain.

Using the same reasoning as that for the water conservation, the sum of all the fluxes inside the domain is 0. The flux through the bottom boundaries is zero. Only the flux at the surface boundary remains. By removing n_z, the integral can be projected onto a flat 2D mesh. Equation 23 becomes

$$\left\langle \frac{\Delta H}{\Delta t} \phi_{j,xy} \right\rangle^{n} = \left\langle \left\langle w_m \phi_{j,xy} n_z \right\rangle \right\rangle_{\Gamma_s}^{n} \tag{24}$$

$$= \left\langle w_m \phi_{j,xy} \right\rangle_{\Gamma_s,2D}^{n} \tag{25}$$

This shows that w_m at the surface matches the temporal evolution of the sea surface elevation between two 3D time steps. Thanks to the P_1^{DG} discretisation, this equality is satisfied for each node i at machine precision.

By analysing the equation of w, recalled below, the impermeability of the surface can now be demonstrated:

$$-\left\langle w \frac{\partial \phi_i}{\partial z} \right\rangle^{n} + \left\langle \left\langle \{w\} \phi_i n_z \right\rangle \right\rangle_{\Gamma_h}^{n} = \left\langle \mathbf{u} \cdot \boldsymbol{\nabla} \phi_i \right\rangle^{n} - \left\langle \left\langle \{\mathbf{u} \cdot \mathbf{n}_h\} \phi_i \right\rangle \right\rangle_{\Gamma_h \cup \Gamma_v}^{n}$$

Applying the same reasoning as for the previous equations, the equation of the vertical velocity recalled above yields

$$\left\langle \left\langle w \phi_{j,xy} n_z \right\rangle \right\rangle_{\Gamma_s}^{n} + \left\langle \left\langle \{\mathbf{u} \cdot \mathbf{n}_h\} \phi_{j,xy} \right\rangle \right\rangle_{\Gamma_s}^{n} = \left\langle H \mathbf{u} \cdot \boldsymbol{\nabla} \phi_{j,xy} \right\rangle^{n} - \left\langle \left\langle \{H \mathbf{u} \cdot \mathbf{n}_h\} \phi_{j,xy} \right\rangle \right\rangle_{\Gamma_v}^{n} \tag{26}$$

The RHS of the previous equation is actually the RHS of the discretised water height equation (Equation 18a). As the equation of H is linear in the discret field $\mathbf{U} = \mathrm{H}\bar{\mathbf{u}}$,

$$\frac{\partial H}{\partial t} = -\boldsymbol{\nabla}_h \cdot \mathbf{U},$$

by using the temporal mean of $\mathbf{U}$ over all the 2D small time steps in $\mathbf{u}$, $\mathbf{U}_{\text{mean}}$, this gives

$$\left\langle \left\langle w \phi_{j,xy} n_z \right\rangle \right\rangle_{\Gamma_s}^{n} + \left\langle \left\langle \mathbf{u} \cdot \mathbf{n}_h \phi_{j,xy} \right\rangle \right\rangle_{\Gamma_s}^{n} = \left\langle \frac{\Delta H}{\Delta t} \phi_{j,xy} \right\rangle^{n} \tag{27}$$

$$= \left\langle \left\langle w_m \phi_{j,xy} n_z \right\rangle \right\rangle_{\Gamma_s}^{n} \tag{28}$$

By putting all the terms in the LHS and by introducing w_m, it becomes :

$$\left\langle\left\langle w\phi_{j,xy}n_z \right\rangle\right\rangle_{\Gamma_s}^{n} + \left\langle\left\langle \mathbf{u}\cdot\mathbf{n}_h\phi_{j,xy} \right\rangle\right\rangle_{\Gamma_s}^{n} - \left\langle\left\langle w_m\phi_{j,xy}n_z \right\rangle\right\rangle_{\Gamma_s}^{n} = 0 \tag{29}$$

This shows that the flux at the surface is zero for the weak formulation. In others words, the impermeability of the surface boundary represented by Equation 12b is satisfied by the weak formulation. In practice, to verify the top surface condition, two choices were made. Firstly, the temporally averaged 2D velocity, denoted $\mathbf{U}_{\text{mean}}$, is used in the tracer equation and in the computation of the vertical velocity on each 3D sub-time step. Secondly, in the advection term of the tracer equation, $h_v\mathbf{u}$ and h_v are used instead of $\mathbf{u}$ and the stability 3D terms are added to match the vertical velocity equation. In others words, the velocity field used is

$$h\mathbf{u} = h_{\text{mean}}\bar{\mathbf{u}}_{\text{mean}} + h_n\tilde{\mathbf{u}}_n$$

3.5.3. Conservation and Tracer consistency

The tracer equation is analysed to check the tracer conservation in a closed domain. For the sake of clarity, the diffusion terms are omitted but the same reasoning applied. The demonstration is done with one big time step like in the previous section. The tracer equation without the diffusion terms reads

$$\begin{aligned}\frac{\left\langle T\phi_i \right\rangle^{n+1} - \left\langle T\phi_i \right\rangle^{n}}{\Delta t} =& \left\langle \mathbf{u}T\cdot\boldsymbol{\nabla}\phi_i \right\rangle^{n} - \left\langle\left\langle T^{up}\left\{\mathbf{u}\cdot\mathbf{n}_h\right\}\phi_i \right\rangle\right\rangle_{(\Gamma_h\cup\Gamma_v)-\Gamma_s}^{n} \\ & \left\langle (w-w_m)T\frac{\partial\phi_i}{\partial z} \right\rangle^{n} - \left\langle\left\langle \left\{w-w_m\right\}T^{up}\phi_i n_z \right\rangle\right\rangle_{\Gamma_h-\Gamma_s}^{n}\end{aligned} \tag{30}$$

where the flux at the surface, Γ_s, is removed because it is null as demonstrated above. The fluxes at the vertical boundaries are null. The flux at the bottom is also null. The Galerkin finite element being a conservative methods, the total tracer quantity is conserved in the domain.

To check the consistency, one should demonstrate that if the tracer concentration is uniform, it remains uniform. By putting the tracer concentration equals to 1 everywhere in the domain at time n and adding the surface flux (which is null), the Equation 30 becomes

$$\begin{aligned}\frac{\left\langle T\phi_i \right\rangle^{n+1} - \left\langle \phi_i \right\rangle^{n}}{\Delta t} =& \left\langle \mathbf{u}\cdot\boldsymbol{\nabla}\phi_i \right\rangle^{n} - \left\langle\left\langle \left\{\mathbf{u}\cdot\mathbf{n}_h\right\}\phi_i \right\rangle\right\rangle_{\Gamma_h\cup\Gamma_v}^{n} \\ & \left\langle (w-w_m)\frac{\partial\phi_i}{\partial z} \right\rangle^{n} - \left\langle\left\langle \left\{w-w_m\right\}\phi_i n_z \right\rangle\right\rangle_{\Gamma_h}^{n}\end{aligned}$$

The diffusion terms can be omitted because the gradient of a uniform fields is null. Using Equation 16, it becomes

$$\frac{\left\langle T\phi_i \right\rangle^{n+1} - \left\langle \phi_i \right\rangle^{n}}{\Delta t} = -\left\langle w_m\frac{\partial\phi_i}{\partial z} \right\rangle^{n} + \left\langle\left\langle \left\{w_m\right\}\phi_i n_z \right\rangle\right\rangle_{\Gamma_h}^{n}$$

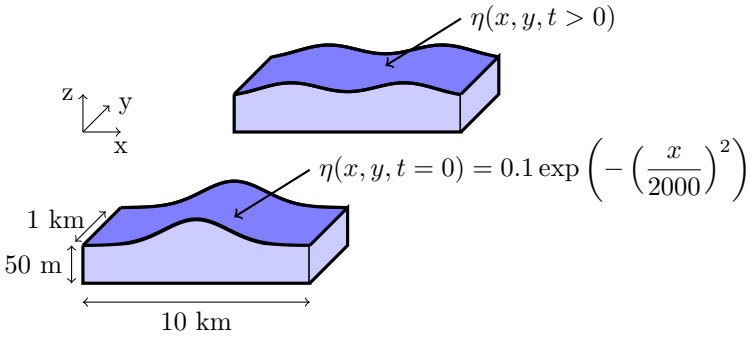

Figure 5: Evolution of the surface gravity waves testcase

By looking at the equation of w_m, the only solution for the concentration of the tracer at time $n+1$ over the domain is 1.

4. Numerical tests and results

The 3D model is assessed by a set of numerical benchmarks. A first barotropic test checks the conservation and the consistency properties. Then, three test cases of increasing complexity demonstrate the precision of the proposed temporal scheme. A lock exchange test case evaluate the numerical mixing of the the baroclinic solver in the z-direction. The correct size of the vortices produced by instabilities in a rotating baroclinic benchmark demonstrates the small amount of numerical dispersion introduced by the discrete model. Another more difficult instability test case confirms the presumed order of the global scheme.

4.1. Surface gravity waves

To check the conservation and the consistency of our model, Kärnä et al. (2013) is a very good candidate because this test is simple and smooth. It allows the properties to be checked easily. Moreover, the tracer is a passive scalar field.

The propagation of surface gravity waves in a 10 km long and 1 km wide rectangular domain is considered. The depth is 50 m. All the vertical boundaries are impermeable. Bottom friction and vertical diffusion are omitted. The water density is constant throughout the simulation as illustrated. The free surface perturbation is initially set to the following function :

$$\eta(x, y, 0) = 0.1 \exp\left(-\left(\frac{x}{2000}\right)^2\right)$$

The horizontal and vertical resolution of the grid are 100 m and 2.5 m. The 3D time step is 10s while the 2D one is 0.33s. Simulation is performed with 800 3D time steps in order to reproduce the same result as Kärnä et al. (2013). For a field f and a reference field f^{ref}, the error on the domain Ω is computed with the L_2 norm as follows :

$$E = \|f - f^{ref}\|_{L_2} = \sqrt{\int_\Omega (f - f^{ref})^2 d\Omega}$$

In the first run, the tracer is set at a initial constant value $T_0 = 4$ PSU. Then, the simulation is launched with a non-constant tracer. It is set to 3 PSU at the surface and 4 PSU at the bottom with a linear transition. In both case, the tracer extrema deviation is of the order of 10^{-9}. This shows the consistency of the scheme. Regarding the conservation, the total water and tracer volume remains the same at the order of 10^{-13}.

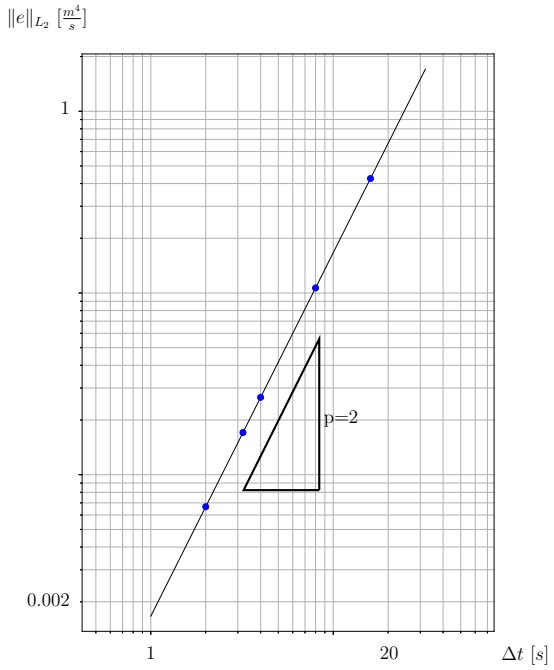

Figure 6: Convergence analysis of the L_2 error on u in the surface gravity wave test case. The reference time step is 0.16 s. Tested time steps are 16, 8, 4 and 3.2 s.

A convergence analysis of the temporal scheme is performed using a constant tracer. The horizontal resolution is 140 m with 5 layers in the z-direction. The simulation is running for 1600 s with the following set of Δt : [16, 8, 4, 3.2, 2, 0.16] s and M=18. The solution obtained with the smallest time resolution is used as a reference. The theoretical second order convergence is observed in Figure 6.

4.2. Lock Exchange

The lock exchange test case is used to estimate the model spurious numerical vertical diffusion in a simple configuration where the solution is not too complex.

Initially, one half of the domain is filled with cold water (T = 5°C) while the other half is filled with hot water (T = 30°). The test case is a density driven flow. Warm water flows over the cold water. This is the setup of Ilıcak et al. (2012) and Petersen et al. (2015). The domain is a 1 km wide and 64 km long box. The depth is 20 m. Closed boundaries conditions are imposed in the x-direction while the domain is periodic in the y-direction. The density is a function of the temperature only, so that Equation 9 becomes

$$\rho = 1000 - 0.2(T - 5)$$

resulting in a density difference of $\Delta\rho = -5.0$ kg m^{-3}. The friction at the bottom of the domain is omitted. Tracer diffusion is set to 0. In the absence of bottom friction, assuming that all the potential energy is transformed into kinetic energy, Benjamin (1968) estimated the maximum speed of front propagation, using Bernoulli's equation for an ideal fluid, as

$$c = \frac{1}{2}\sqrt{gH\frac{\Delta\rho}{\rho_0}}$$

which is 0.495 ms^{-1} in this situation.

The mesh Reynolds numbers is defined by

$$Re_h = U\frac{\Delta x}{\nu_h}$$

where the characteristic velocity scale is $U = 0.5$ ms^{-1} and the grid horizontal and vertical resolution are 0.5 km and 1 m. The numerical instabilities due to internal pressure gradient are stabilized with a constant horizontal viscosity ν_h. Three runs are performed with $\nu_h = 1.0$ m^2s^{-1}, 10.0 m^2s^{-1}, and 100.0 m^2s^{-1}, corresponding respectively to $Re_h = U\frac{\Delta x}{\nu_h}$, of 250, 25, 2.5 .

Figure 7 shows the initial deviation density field and the solution after 17h. Smaller mesh Reynolds number, i. e. higher horizontal viscosity, leads to a less noisy density front. The smooth interface between the dense and the light water produces less mixing. This speed gives a right front location at 62.3 km at 17h of simulation. For $\nu_h = 100$ m^2s^{-1}, 10 m^2s^{-1} and 1 m^2s^{-1}, the front is at 61 km, 60.75 km and 60.5 km respectively. When the interface became noisy, this means that a part of the potential energy is wasted in the noise. Thereferore, the speed of front propagation is reduced. This explains the front locations. As show in Figure 7, those results are similar to those presented in Kärnä et al. (2018), Petersen et al. (2015) and Ilıcak et al. (2012). Without the complications of topography, Coriolis force, bottom drag and surface forcing, and providing a sufficiently large horizontal viscosity is used, the model exhibits an admissible vertical mixing.

4.3. Baroclinic eddies

The baroclinic eddies test case of Ilıcak et al. (2012) is used to check the model's ability to generate baroclinic eddies as well as its precision. Generating eddies of an appropriate size means that the temporal scheme of the model does not produce too much dissipation. Compared to the previous case, a fully 3D rotating flow is introduced.

This test represents an idealisation of the Antartic Circumpolar Current. A unstable sinusoidal front separates cold water from hot water. Vortices develop at the front in function of the horizontal viscosity. The Coriolis parameter is taken as a constant -1.2 $\times$ 10^{-4} s^{-1}. The domain is a three dimensional box, 500 km long delimited by impermeable boundaries in the meridional direction (y) and 160 km large with periodic boundaries in the zonal (x) direction. The depth is 1000 m. The quadratic bottom drag is defined :

$$\frac{\boldsymbol{\tau}_b}{\rho_0} = C_d|\mathbf{u}_b|\mathbf{u}_b$$

where $\mathbf{u}_b$ is the horizontal velocity of the bottom element taken at the middle point and C_d is 0.01. The density function is the same as in the previous test case. Salinity and vertical viscosity are again set at the same constant value.

The mesh is shown in Figure 8 to illustrate the domain. The simulation is performed in horizontal grid resolution of 4 km and the horizontal viscosity from 20 m^2s^{-1} to 200 m^2s^{-1}. The characteristic speed being 0.1 ms^{-1}, this gives a mesh Reynolds numbers respectively from 20 to 2. The vertical resolution of the grid is 50 m.

The initial temperature field can be seen in Figure 9. Warmer surface temperature in the north is separated from colder surface temperature in the south by a sinusoidal transition band in the x-y plane. The temperature distribution in the north of the domain is a linear increasing function from the bottom :

$$T_0(z) = T_{bot} + (T_{top} - T_{bot})\frac{z_{bot} - z}{z_{bot}} \tag{31}$$

where $T_{bot} = 10.1°C$, $T_{top} = 13.1°C$, and z_{bot} = -975 m. The south part of the domain is uniformly cooler at $\Delta T = 1.2°C$. The wide boundary is defined by

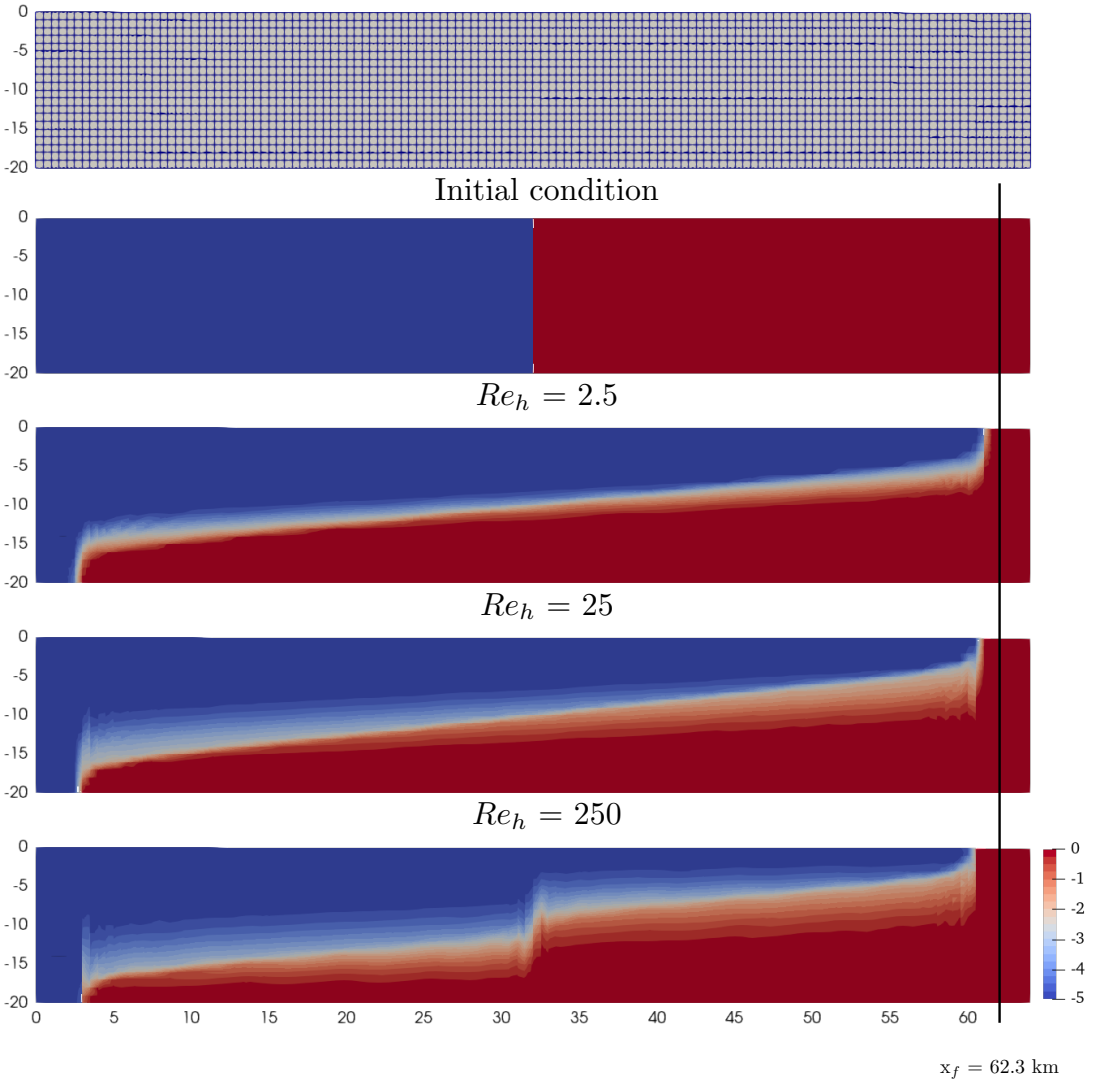

Figure 7: Water deviation density, ρ' $[kg/m^3]$, in the lock exchange test case for Z-X plane. At the top, we have the vertical mesh from the horizontal extruded mesh and the initial condition. We have successively the solution after 17h of simulation with respectively Re_h and ν_h : 2.5 - 100 $\mathrm{m^2 s^{-1}}$, 25 - 10 $\mathrm{m^2 s^{-1}}$, 250 - 1 $\mathrm{m^2 s^{-1}}$. The vertical line shows the theoretical position of the front

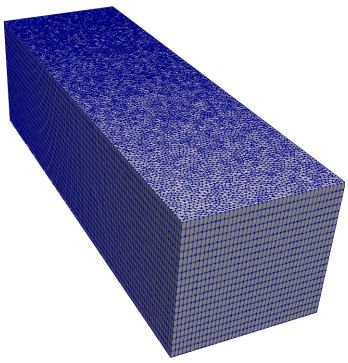

Figure 8: Mesh of the computational domain of dimension 500 km x 150 km x 1 km. Number of 2D elements is 13686. Number of layers is 20.

$$y_w(x) = y_0 - y_A \sin\left(2\pi k \frac{x}{L_x}\right) \tag{32}$$

where $y_0 = 250$ km, $y_A = 40$ km, k = 3 and $L_x = 160$ km so that there is three wavelengths of width L_x in a domain. This gives the following temperature distribution

$$T(x,y,z) = \begin{cases} T_0(z) & y_w(x) + \Delta y \leq y \\ T_0(z) - \Delta T \left(1 - \frac{y - y_w(x)}{\Delta y}\right) & y_w < y \leq y_w(x) + \Delta y \\ T_0(z) - \Delta T & y \leq y_w(x) \end{cases} \tag{33}$$

where $\Delta y = 40$ km and $\Delta T = 1.3°$C. An additional perturbation is added to one of the wave crest to stimulate the instability

$$y'_w(x) = y_0 - \frac{y_A}{2} \sin\left(\pi \frac{x - x_2}{x_3 - x_2}\right) \tag{34}$$

$$T'(x,y) = \Delta T' \left(1 - \frac{y - y'_w(x)}{0.5\Delta y}\right) \tag{35}$$

that way the temperature is T + T' within the range $x_2 \leq x \leq x_3$, $y'_w - \frac{\Delta y}{2} \leq y \leq y'_w + \frac{\Delta y}{2}$, where $x_2 = 110$ km, $x_3 = 130$ km and $\Delta T' = 0.3°$C.

Figure 10 and Figure 11 show the evolution of the sea surface temperature for two different horizontal viscosities : 20 m^2s^{-1} and 200 m^2s^{-1}. For the high viscosity numbers, the hot and the cold water tend to mix slowly. The velocity field have small values. This generates only a few eddies though these eddies are large and smooth. As time goes by, they dissipate quickly. At day 200, the eddies are less dense. For simulations with low viscosity numbers or bigger Re_h, the flow is much more chaotic and energetic. The eddies appear sooner than the previous ones but are globally smaller. Moreover, as time progresses, the mixing becomes more important. At day 200, for $\nu_h = 200$ m^2s^{-1} two areas can still be distinguished while, for $\nu_h = 20$ m^2s^{-1}, the flow tends to be more homogeneous. These results show that our temporal scheme succeeds in capturing more mesoscale features as viscosity is decreased while rotation is taken into account.

A convergence analysis of the temporal scheme is performed with $\nu_h = 20$ m^2s^{-1}. The horizontal resolution is 20 km with 10 layers in the z-direction. The simulation is running for 2000 s with the following set of Δt : [200, 100, 50, 25, 1.25] s and M=138. The solution obtained with the smallest time resolution is used as a reference. In the model, the vertical terms are treated implicitly in the temporal scheme. All terms,

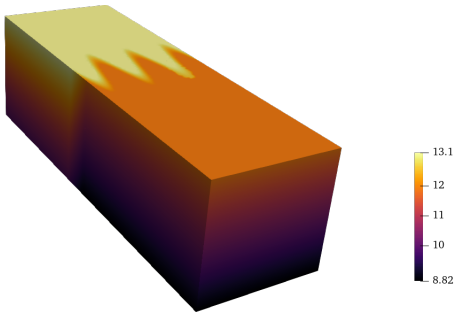

Figure 9: Initial sea temperature field [°C] in the eddying channel test case

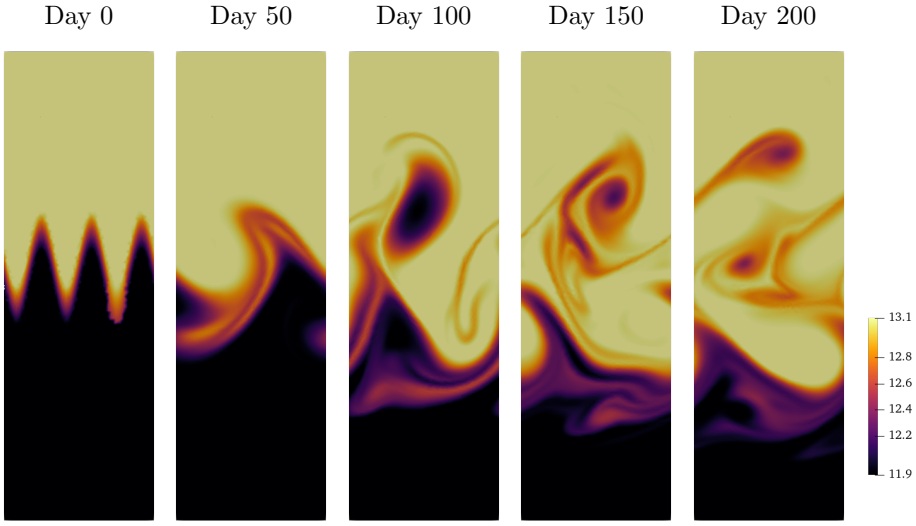

Figure 10: Sea surface temperature field [°C] in the eddying channel test case for respectively Re_h=2 and ν_h=200 $\mathrm{m^2 s^{-1}}$

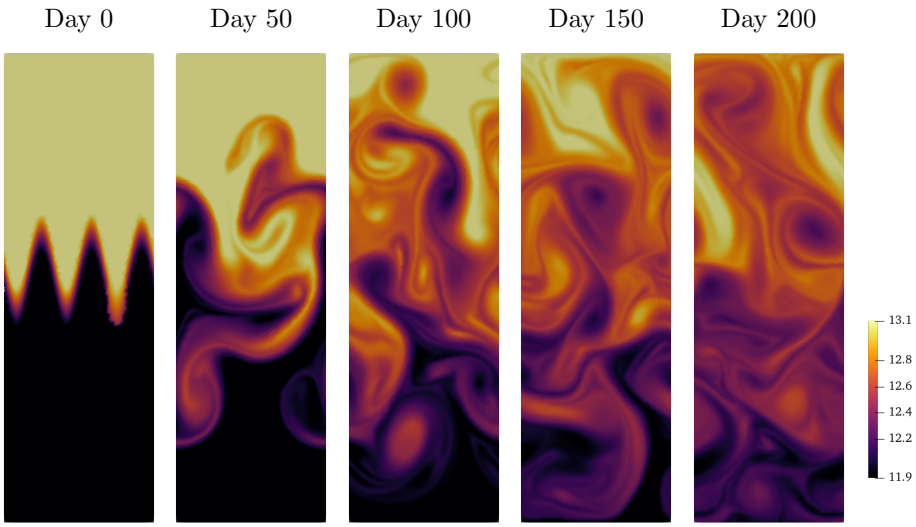

Figure 11: Sea surface temperature field [°C] in the eddying channel test case for respectively Re_h=20 and ν_h=20 $\mathrm{m^2 s^{-1}}$

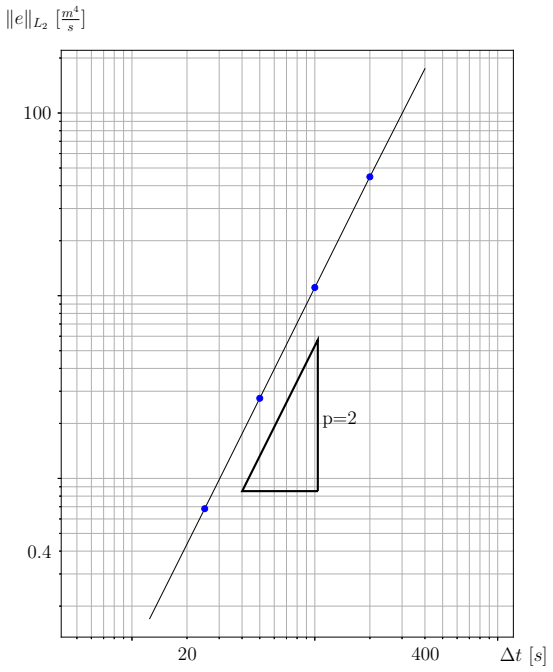

Figure 12: Convergence analysis of the L_2 error on u in the eddies test case. The reference time step is 1.25 s. Tested time steps are 200, 100, 50 and 25 s.

including the vertical terms, are treated explicitly in this convergence analysis. The theoretical second order convergence is observed in Figure 12.

4.4. Eddies in a rotating stratified fluid

The last studied test case shows the ability of the model to handle the geostrophic adjustment of a freshwater cylinder and the development of unstable vortices. By having the right amount of unstable lobes, the order 2 of the temporal scheme can be confirmed. The setup is based on the experiments of Griffiths and Linden (1981) and Saunders (1973) which were numerically modelled by James (1996) and Tartinville et al. (1998) neglecting all forms of mixing.

The represented area is supposed to be located at 52°N and hence the Coriolis parameter is 1.15×10^{-4} s^{-1}. The domain is a box of salty water with a 30 km length for both the x-coordinates and the y-coordinates and a depth of 20 m. All the boundaries are closed. A cylinder of less salty water is put at the center of the top. As time goes by, the light cylindrical core sinks and spread outs until it reaches a state of quasi-geostrophic equilibrium. The vortex can either remain stable and circular or either break up into a well-defined number of vortices depending on the initial parameters of the model.

Unlike the previous test case, the temperature field is set to a constant value while the salinity field represents a 10 m deep, 3 km radius cylinder of concentrated water in the upper part of the box. More precisely, inside the cylinder , the salinity is

$$S = 1.1 \left(\frac{d}{3}\right)^8 + 33.75 \tag{36}$$

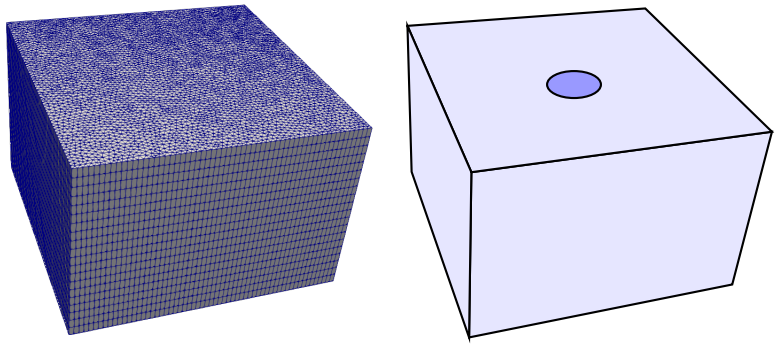

Figure 13: [Left] Mesh of the computational domain of the vortices test case of dimension 30 km x 30 km x 20 m. Number of 2D elements is 5602. Number of layers is 20. [Right] Initial sea salinity field. The lower salinity is inside a 3 km radius and 10 m depth cylinder

with d the distance to the centre of the domain in km. Outside the cylinder, the ambient salinity is 34.85 PSU. The density is, in this case, only influenced by the water salinity which gives $\rho' = 0.78(S - 33.75)$. To use the same parameters as the previous articles focusing on this test case, ρ_0 is changed into 1025 kg m^{-3}. This gives an initial density difference of 0.858 kg m^{-3} between the most concentrated areas and the less ones. Horizontal and vertical viscosity and diffusivity are set to zero. Figure 13 displays the initial situation as well as the 3D mesh. the grid horizontal and vertical size are 0.5 km and 1 m.

The parameters determining the number of vortices can be reduced to a dimensionless number $\theta_0 = g' \frac{H_0}{f^2 R_0^2}$ which represents the ratio between the buoyancy force and the Coriolis force with $g' = g\frac{\Delta\rho}{\rho}$, the reduced gravity, H_0, the initial depth of the cylinder and R_0, the initial radius of the cylinder. The number of vortices called the zonal wavenumber of the instability also depends of these parameters. For this test case, James (1996) found out that the simulation should give a wavenumber 2 instability. Tartinville et al. (1998) have shown most of the models can give the expected spreading of the cylinder and the development of, respectively, anticyclonic circulation in the upper layer and cyclonic one in the lower layer of the domain. However, they have also demonstrated that models with no adequate advection schemes do not succeed in reproducing the 2 wavenumber instability after 144 hours of simulation. they suggested that models with only first-order horizontal advection scheme for momentum failed because the numerical viscosity should induce a too strong decrease of the kinetic energy. To be more precise, they said that the numerical modelling of low-diffusion marine systems where frontal instability processes are important requires the use of at least a second-order discretisation for the advection of momentum. Therefore, an order-four instability is created instead of an order-two one. This test case is not shown a lot because it is quite difficult to obtain the right number of vortices.

Figure 14 shows the evolution of the cylinder through time. The most important result is that the model and the numerical schemes presented in this article achieved to predict a wavenumber 2 instability. As expected after 144 hours, the cylinder breaks up and two vortices are appearing as time goes. Then, cyclonic vorticity appear in each lobe of the disturbance. As the lobes grow, closed cyclonic circulation is being established. These results match the experiments and the conclusions of Griffiths and Linden (1981). As the diffusivity is computed the same way than the viscosity, this demonstrates that the model does not produce an excessive amount of numerical viscosity and diffusivity.

5. Conclusion

This paper focuses on three-dimensional hydrostatic equations under the Boussinesq approximation with a specific emphasis on two different timescales. The hydrodynamic equations considered have a wave propagation speed that is greater than the advection speed, so it is important to choose an appropriate time scheme. A combined RK3 and RK2 scheme is used, and the equations are decomposed into fast and

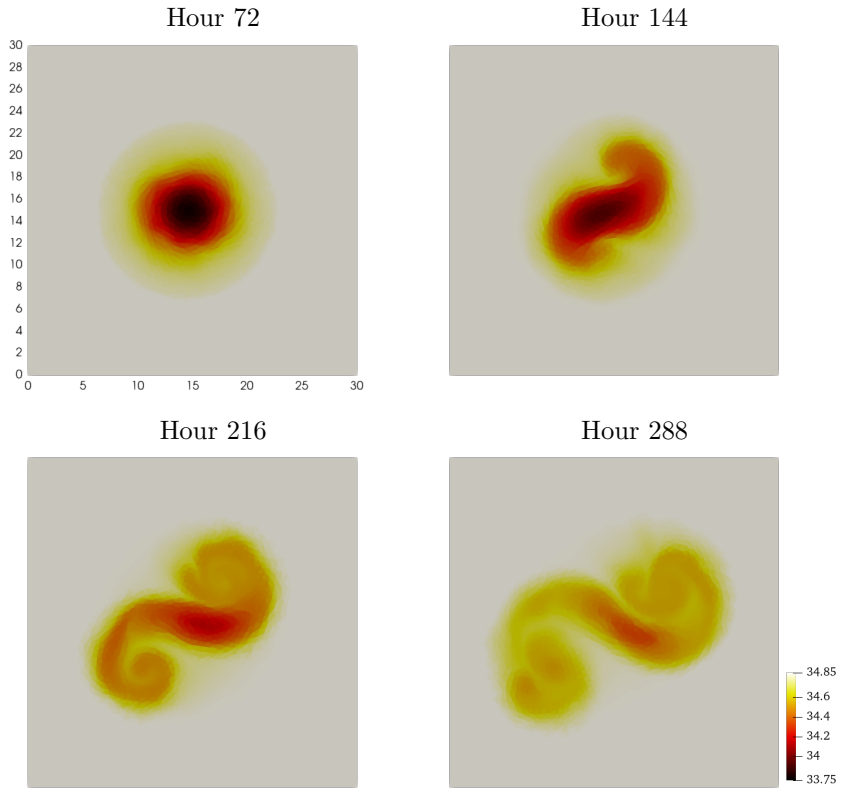

Figure 14: Sea surface salinity field [psu] in the vortices test case during 288 hours

slow terms to allow for spatial discretization using discontinuous Galerkin methods on an unstructured grid. This approach offers several advantages, including easy parallelization for large scale or high resolution applications.

The goal of this approach is to limit numerical dissipation due to spatial and temporal discretization. The scheme is designed to be of order two temporally and spatially and completely discontinuous. This enables the vertical mesh to follow the displacement of the water surface, thereby maintaining the conservation of tracer and water fields throughout the simulations. The tracer is consistent due to the advection velocity field used, which is coherent with the vertical motion of the mesh. A mathematical demonstration has been performed to verify the order and stability of the scheme, demonstrating its effectiveness in accurately simulating hydrodynamic behavior.

To test the model, a gravitational wave benchmark, a lock-exchange, and an eddies producing test cases were used. The numerical results indicate that the proposed scheme achieves the expected numerical spatial accuracy and temporal second order. The scheme's complete discontinuity ensures that both the conservation of the tracer and its consistency are preserved, as well as the conservation of water. The model is able to capture the expected physical behavior, including vortices, instabilities, and eddies, due to the reduction of numerical diffusion.

Furthermore, this new model can be expanded and generalized to any order as long as the splitting is well-done. The temporal splitting could mix any Runge-Kutta method, which can lead to obtaining higher orders of precision. An analysis of the optimal ratio between the two time steps, denoted as M, could be performed to help produce results more quickly with good precision. Overall, this new scheme offers many potential benefits for future use in ocean modeling, especially in large-scale simulations that require high accuracy and efficient computation. In the future, we plan to continue to explore these possibilities and improve the model's accuracy by implementing new equations and techniques, such as the wetting-drying model and the use of GPUs for acceleration.

6. Acknowledgements

Computational resources were provided by the Consortium des Équipements de Calcul Intensif (CÉCI), funded by the Belgian Fund for Scientific Research (F.R.S. FNRS) under grant no. 2.5020.11

Appendix A. Order of precision of the SPEX-RK

The order of precision of the temporal scheme is assessed by calculating the Taylor expansion for each residue. In order to calculate the order of precision of the temporal scheme, the result of a complete RK2 iteration is computed first. For a given k^{slow} and M, the first sub-iteration gives

$$
\begin{aligned}
K_1 &= F_n \\
K_2 &= F(y_n + \frac{\Delta T}{2}\left(F_n + k^{\text{slow}}\right)) \\
&= F_n + \frac{\Delta T}{2}\left(F_n + k^{\text{slow}}\right) F_n^{'} + O(M\Delta T^2) \\
y_1 &= y_n + \Delta T\left(K_2 + k^{\text{slow}}\right) \\
&= y_n + \Delta T\left(F_n + k^{\text{slow}}\right) + \frac{\Delta T^2}{2}\left(F_n + k^{\text{slow}}\right) F_n^{'} + O(M^3\Delta T^3)
\end{aligned}
$$

The second sub-iteration yield

$$
\begin{aligned}
K_1 &= F_n + O(M\Delta T) \\
K_2 &= F(y_1 + \frac{\Delta T}{2}\left(F_n + k^{\text{slow}}\right)) \\
&= F_n + \frac{3\Delta T}{2}\left(F_n + k^{\text{slow}}\right) F_n^{'} + O(M^2\Delta T^2) \\
y_2 &= y_1 + \Delta T\left(K_2 + k^{\text{slow}}\right) \\
&= y_n + 2\Delta T\left(F_n + k^{\text{slow}}\right) + \frac{4\Delta T^2}{2}\left(F_n + k^{\text{slow}}\right) F_n^{'} + O(M^3\Delta T^3)
\end{aligned}
$$

By recurrence, the last iteration produces the solution

$$
y_M = y_n + M\Delta T\left(F_n + k^{\text{slow}}\right) + \frac{M^2\Delta T^2}{2}\left(F_n + k^{\text{slow}}\right) F_n^{'} + O(M^3\Delta T^3)
$$

This result is denoted $RK2(k^{\text{slow}}, M)$. To determine the order of accuracy of the global method, the RK3 method is unrolled.

$$
\begin{aligned}
y_1 &= y_n \\
y_2 &= RK2(k_1^{\text{slow}}, \frac{M}{3}) \\
&= y_n + \frac{M}{3}\Delta T\left(F_n + f_n\right) + \left(\frac{M}{3}\right)^2 \frac{\Delta T^2}{2}\left(F_n + f_n\right) F_n^{'} + O(M^3\Delta T^3) \\
y_3 &= RK2\left(k_2^{\text{slow}}, \frac{M}{2}\right) \\
&= y_n + \frac{M}{2}\Delta T\left(F_n + f_n + \frac{M}{3}\Delta T(F_n + f_n) f_n^{'}\right) + \left(\frac{M}{2}\right)^2 \frac{\Delta T^2}{2}\left(F_n + f_n\right) F_n^{'} + O(M^3\Delta T^3) \\
&= y_n + \frac{M}{2}\Delta T\left(F_n + f_n\right) + \left(\frac{M}{2}\right)^2 \frac{\Delta T^2}{2}\left(F_n + f_n\right)\left(F_n^{'} + \frac{4}{3} f_n^{'}\right) + O(M^3\Delta T^3) \\
y_{n+1} &= RK2\left(k_3^{\text{slow}}, M\right) \\
&= y_n + M\Delta T\left(F_n + f_n + \frac{M}{2}\Delta T(F_n + f_n) f_n^{'}\right) + M^2\frac{\Delta T^2}{2}\left(F_n + f_n\right) F_n^{'} + O(M^3\Delta T^3) \\
&= y_n + M\Delta T\left(F_n + f_n\right) + M^2\frac{\Delta T^2}{2}\left(F_n + f_n\right)\left(F_n^{'} + f_n^{'}\right) + O(M^3\Delta T^3)
\end{aligned}
$$

with $M\Delta T = \Delta t$

Appendix B. Factor amplification of the SPEX-RK

Typically, to determine the stability of a numerical method, it is standard practice to analyze the linear form of the underlying ordinary differential equation. In this particular case, the linear ordinary differential equation is given by Equation

$$
\frac{\mathrm{d}y}{\mathrm{d}t} = \lambda y + \Lambda y \tag{37}
$$

where λ and Λ represent the complex coefficients of the linear functions $f(y)$ and $F(y)$, respectively.

First, the complete RK2 iteration is calculated with a given k^{slow} and M. The initial sub-iteration produces the values for K_1, K_2, and y_1.

$$\begin{aligned}
K_1 &= \Lambda y_n \\
K_2 &= \Lambda(y_n + \frac{\Delta T}{2}\left(\Lambda y_n + k^{\text{slow}}\right)) \\
&= y_n(\Lambda + \Lambda^2\frac{\Delta T}{2}) + k^{\text{slow}}\Lambda\frac{\Delta T}{2} \\
y_1 &= y_n(1 + \Lambda\Delta T + \Lambda^2\frac{\Delta T^2}{2}) + k^{\text{slow}}\left(\Delta T + \Lambda\frac{\Delta T^2}{2}\right)
\end{aligned}$$

The subsequent sub-iteration produces y_2, y_3, and so on, until the last iteration is reached, which is y_M.

$$\begin{aligned}
y_2 &= y_1(1 + \Lambda\Delta T + \Lambda^2\frac{\Delta T^2}{2}) + k^{\text{slow}}\left(\Delta T + \Lambda\frac{\Delta T^2}{2}\right) \\
&= y_n(1 + \Lambda\Delta T + \Lambda^2\frac{\Delta T^2}{2})^2 + k^{\text{slow}}\left(\Delta T + \Lambda\frac{\Delta T^2}{2}\right)\left(1 + (1 + \Lambda\Delta T + \Lambda^2\frac{\Delta T^2}{2})\right) \\
y_3 &= y_2(1 + \Lambda\Delta T + \Lambda^2\frac{\Delta T^2}{2}) + k^{\text{slow}}\left(\Delta T + \Lambda\frac{\Delta T^2}{2}\right) \\
&= y_n(1 + \Lambda\Delta T + \Lambda^2\frac{\Delta T^2}{2})^3 + k^{\text{slow}}\left(\Delta T + \Lambda\frac{\Delta T^2}{2}\right)\left(1 + (1 + \Lambda\Delta T + \Lambda^2\frac{\Delta T^2}{2}) + (1 + \Lambda\Delta T + \Lambda^2\frac{\Delta T^2}{2})^2\right)
\end{aligned}$$

By recurrence, the last iteration gives

$$\begin{aligned}
y_M &= y_n(1 + \Lambda\Delta T + \Lambda^2\frac{\Delta T^2}{2})^M + k^{\text{slow}}\Lambda\frac{\Delta T^2}{2}\sum_{i=0}^{M-1}(1 + \Lambda\Delta T + \Lambda^2\frac{\Delta T^2}{2})^i \\
&= y_n A^M + k^{\text{slow}}\left(\Delta T + \Lambda\frac{\Delta T^2}{2}\right)\left(\frac{1 - A^M}{1 - A}\right)
\end{aligned}$$

with $A = 1 + \Lambda\Delta T + \Lambda^2\frac{\Delta T^2}{2}$ and $\Lambda \neq 0$, $\Delta T \neq 0$. This result is denoted $RK2(k^{\text{slow}}, M)$ and it serves as the basis for deriving the amplification factor of the global method by unrolling the RK3.

$$
\begin{aligned}
y_1 &= y_n \\
y_2 &= RK2\left(k_1^{\text{slow}}, \frac{M}{3}\right) \\
&= y_n A^{\frac{M}{3}} + \lambda y_n \left(\Delta T + \Lambda \frac{\Delta T^2}{2}\right)\left(\frac{1-A^{\frac{M}{3}}}{1-A}\right) \\
&= y_n \left(A^{\frac{M}{3}} + \lambda \left(\Delta T + \Lambda \frac{\Delta T^2}{2}\right)\left(\frac{1-A^{\frac{M}{3}}}{1-A}\right)\right) \\
y_3 &= RK2\left(k_2^{\text{slow}}, \frac{M}{2}\right) \\
&= y_n A^{\frac{M}{2}} + \lambda y_n \left(A^{\frac{M}{3}} + \lambda \left(\Delta T + \Lambda \frac{\Delta T^2}{2}\right)\left(\frac{1-A^{\frac{M}{3}}}{1-A}\right)\right)\left(\Delta T + \Lambda \frac{\Delta T^2}{2}\right)\left(\frac{1-A^{\frac{M}{2}}}{1-A}\right) \\
&= y_n \left(A^{\frac{M}{2}} + \lambda A^{\frac{M}{3}} \left(\Delta T + \Lambda \frac{\Delta T^2}{2}\right)\left(\frac{1-A^{\frac{M}{2}}}{1-A}\right) + \lambda^2 \left(\Delta T + \Lambda \frac{\Delta T^2}{2}\right)^2 \left(\frac{1-A^{\frac{M}{3}}}{1-A}\right)\left(\frac{1-A^{\frac{M}{2}}}{1-A}\right)\right) \\
y_3 &= RK2\left(k_3^{\text{slow}}, M\right) \\
&= y_n \left(A^{M} + \lambda A^{\frac{M}{2}} \left(\Delta T + \Lambda \frac{\Delta T^2}{2}\right)\left(\frac{1-A^{M}}{1-A}\right) + \lambda^2 A^{\frac{M}{3}} \left(\Delta T + \Lambda \frac{\Delta T^2}{2}\right)^2 \left(\frac{1-A^{\frac{M}{2}}}{1-A}\right)\left(\frac{1-A^{M}}{1-A}\right)\right. \\
&\left. + \lambda^3 \left(\Delta T + \Lambda \frac{\Delta T^2}{2}\right)^3 \left(\frac{1-A^{\frac{M}{3}}}{1-A}\right)\left(\frac{1-A^{\frac{M}{2}}}{1-A}\right)\left(\frac{1-A^{M}}{1-A}\right)\right)
\end{aligned}
$$

References

Benjamin, T.B., 1968. Gravity currents and related phenomena. Journal of Fluid Mechanic 31, 209–248. URL: https://doi.org/10.1017/S0022112068000133.

Berger, R.C., Howington, S.E., 2002. Discrete fluxes and mass balance in finite elements. Journal of Hydraulic Engineering 128, 87–92. URL: https://doi.org/10.1061/(ASCE)0733-9429(2002)128:1(87).

Bleck, R., Smith, L., 1990. A wind-driven isopycnic coordinate model of the north and equatorial atlantic ocean 1. model and suporting experiments. Journal of Geophyscal Research 95, 3273–3285. URL: https://doi.org/10.1029/JC095iC03p03273.

Blumberg, A., Mellor, G., 1987. A description of a three-dimensional coastal ocean model, in: Three dimensional coastal ocean models. American Geophysical Union 69, 1–16. URL: https://doi.org/10.1029/CO004p0001.

Burchard, H., Rennau, H., 2008. Comparative quantification of physically and numerically induced mixing in ocean models. Ocean modelling 20, 293–311. URL: https://doi.org/10.1016/j.ocemod.2007.10.003.

Campin, J.M., Adcroft, A., Hill, C., Marshall, J., 2004. Conservation of properties in a free-surface model. Ocean Modelling 6, 221–244. URL: https://doi.org/10.1016/S1463-5003(03)00009-X.

Chen, C., Liu, H., Beardsley, R., 2003. An unstructured grid, finite-volume, three-dimensional, primitive equations ocean model: Application to coastal ocean and estuaries. Journal of Atmospheric and Oceanic Technology 20, 159–186. URL: https://doi.org/10.1175/1520-0426(2003)020%3C0159:AUGFVT%3E2.0.CO;2.

Clare, M.C.A., Wallwork, J.G., Kramer, S.C., Weller, H., Cotter, C.J., Piggott, M.D., 2022. Multi-scale hydro-morphodynamic modelling using mesh movement methods. International Journal on Geomathematics 13 (2), 1869–2680. URL: https://doi.org/10.1007/s13137-021-00191-1.

Comblen, R., Blaise, S., Legat, V., Remacle, J., Deleersnijder, E., Lambrechts, J., 2010. A discontinuous finite element baroclinic marine model on unstructured prismatic meshes. Ocean Modelling 60, 1395–1414. URL: https://doi.org/10.1007/s10236-010-0357-4.

Danilov, S., Wang, Q., Losch, M., Sidorenko, D., Schröter, J., 2008. Modeling ocean circulation on unstructured meshes: comparison of two horizontal discretizations. Ocean modelling 58, 365–374. URL: https://doi.org/10.1007/s10236-008-0138-5.

Deleersnijder, E., 1993. Numerical mass conservation in a free-surface sigma coordinate marine model with mode splitting. Journal of Marine Systems 4, 365–370. URL: https://doi.org/10.1016/0924-7963(93)90021-D.

Deleersnijder, E., Campin, J.M., 1995. On the computation of the barotropic mode of a free-surface world ocean model. Annales Geophysicae 13, 675–688. URL: https://doi.org/10.1007/s00585-995-0675-x.

Deleersnijder, E., Lermusiaux, P., 2008. Multi-scale modelling: Nested grid and unstructured mesh approaches. Ocean modelling 58, 335–498. URL: https://doi.org/10.1007/s10236-008-0170-5.
Dobbelaere, T., Curcic, M., Hénaffc, M.L., Hanert, E., 2022. Impacts of hurricane irma (2017) on wave-induced ocean transport processes. Ocean Modelling 171, 1463–5003. URL: https://doi.org/10.1016/j.ocemod.2022.101947.
Dukowicz, J.K., Smith, R.D., 1994. Implicit free-surface method for the bryan-cox-semtner ocean model. Journal of Geophysical Research 99, 235–256. URL: https://doi.org/10.1029/93JC03455.
Fringer, O., Gerritsen, M., Street, R., 2006. An unstructured-grid, finite-volume, nonhydrostatic, parallel coastal ocean simulator. Ocean modelling 14, 139–173. URL: https://doi.org/10.1016/j.ocemod.2006.03.006.
Fringer, O.B., Dawson, C.N., c, R.H., d, D.K.R., Zhang, Y.J., 2019. The future of coastal and estuarine modeling: Findings from a workshop. Ocean modelling 143, 1463–5003. URL: https://doi.org/10.1016/j.ocemod.2019.101458.
Gadd, A.J., 1978. A split explicit integration scheme for numerical weather prediction. Quarterly Journal of the Royal Meteorological Society 104, 569–582. URL: https://doi.org/10.1002/qj.49710444103.
Gadd, A.J., 1980. Two refinements of the split explicit integration scheme. Quarterly Journal of the Royal Meteorological Society 106, 215–220. URL: https://doi.org/10.1002/qj.49710644715.
Geyer, M.C., MacCready, P., 2014. The estuarine circulation. Annual Review of Fluid Mechanics 46, 175–197. URL: https://doi.org/10.1146/annurev-fluid-010313-141302.
Griffies, S.M., Gnanadesikan, A., Dixon, K.W., Dunne, J.P., Gerdes, R., Harrison, M.J., Rosati, A., Russell, J.L., Samuel, B.L., Spelman, M.J., Winton, M., Zhang, R., 2005. Formulation of an ocean model for global climate simulations. Ocean modelling 1, 45–79. URL: https://doi.org/10.5194/os-1-45-2005.
Griffiths, R.W., Linden, P.F., 1981. The stability of vortices in a rotating, stratified fluid. Journal of Fluid Mechanic 105, 283–316. URL: https://doi.org/10.1017/S0022112081003212.
Hiester, H., Piggot, M., Farrell, P., Allison, P., 2014. Assessment of spurious mixing in adaptive mesh simulations of the two-dimensional lock-exchange. Ocean modelling 73, 30–44. URL: https://doi.org/10.1016/j.ocemod.2013.10.003.
Hofmeister, R., Burchard, H., Beckers, J.M., 2010. Non-uniform adaptive vertical grids for 3d numerical ocean models. Ocean modelling 33, 70–86. URL: https://doi.org/10.1016/j.ocemod.2009.12.003.
Ilıcak, M., Adcroft, A.J., Griffies, S.M., Hallberg, R.W., 2012. Spurious dianeutral mixing and the role of momentum closure. Ocean Modelling 45–46, 37–58. URL: https://doi.org/10.1016/j.ocemod.2011.10.003.
James, I.D., 1996. Advection schemes for shelf sea models. Journal of Marine Systems 8, 237–254. URL: https://doi.org/10.1016/0924-7963(96)00008-5.
Kärnä, T., Baptista, A.M., 2016. Evaluation of a long-term hindcast simulation for the columbia river estuary. Ocean moddeling 99, 1–14. URL: https://doi.org/10.1016/j.ocemod.2015.12.007.
Kärnä, T., Baptista, A.M., Lopez, J.E., Turner, P.J., McNeil, C., Sanford, T.B., 2015. Numerical modeling of circulation in high-energy estuaries: A columbia river estuary benchmark. Ocean modelling 88, 54–71. URL: https://doi.org/10.1016/j.ocemod.2015.01.001.
Kärnä, T., Kramer, S.C., Mitchell, L., Ham, D.A., Piggot, M.D., Baptista, A.M., 2018. Thetis coastal ocean model: discontinuous Galerkin discretization for the three-dimensional hydrostatic equations. Geoscientific Model Development 1, 4359–4382. URL: https://doi.org/10.5194/gmd-11-4359-2018.
Kärnä, T., Legat, V., Deleersnijder, E., 2013. A baroclinic discontinuous Galerkin finite element model for coastal flows. Ocean Modelling 61, 1–20. URL: https://doi.org/10.1016/j.ocemod.2012.09.009.
Killworth, P.D., Webb, D.J., Stainforth, D., Paterson, S.M., 1991. The development of a free-surface bryan-cox-semtner ocean model. Joural of Physical Oceanography 21, 1333–1348. URL: https://doi.org/10.1175/1520-0485(1991)021%3C1333:TDOAFS%3E2.0.CO;2.
Knoth, O., Wensch, J., 2003. On the convergence rate of operator splitting for advection–diffusion–reaction problems. SIAM Journal on Numerical Analysis 41, 1–24.
Knoth, O., Wensch, J., 2013. Generalized split-explicit runge–kutta methods for the compressible euler equations. Monthly Weathr Review 142, 2067–2081. URL: https://doi.org/10.1175/MWR-D-13-00068.1.
Kumar, N., Voulgaris, G., Warner, J.C., Olabarrieta, M., 2012. Implementation of the vortex force formalism in the coupled ocean-atmosphere-wave-sediment transport (coawst) modeling system for inner shelf and surf zone applications. Ocean Modelling 45, 65–95. URL: https://doi.org/10.1016/j.ocemod.2012.01.003.
Lermusiaux, P.F.J., Schröter, J., Danilov, S., Iskandarani, M., Pinardi, N., Westerink, J.J., 2013. Multiscale modeling of coastal, shelf, and global ocean dynamics. Ocean modelling 63, 1341—-1344. URL: https://doi.org/10.1007/s10236-013-0655.
MacCready, P., Geyer, M.C., 2010. Advances in estuarine physics. Annual Review of Marine Science 2, 35–58. URL: https://doi.org/10.1146/annurev-marine-120308-081015.
MacCready, P., Geyer, M.C., Burchard, ., 2018. Estuarine exchange flow is related to mixing through the salinity variance budget. Journal of Physical Oceanography 48, 1375–1384. URL: https://doi.org/10.1175/JPO-D-17-0266.1.
Marshall, J., Hill, C., Perelman, L., Adcroft, A., 1997. Hydrostatic, quasi-hydrostatic, and nonhydrostatic ocean modelling. Journal of Geophysical Research 102, 5733–5752. URL: https://doi.org/10.1029/96JC02776.
Nilsen, J.E.O., Loseth, O., 1993. A time-splitting method for the numerical simulation of the navier-stokes equations. Journal of Computational Physics 109, 1–32.
Pan, W., Kramer, S.C., Piggott, M.D., 2019. Multi-layer non-hydrostatic free surface modelling using the discontinuous galerkin method. International Journal on Geomathematics 134, 68–83. URL: https://doi.org/10.1016/j.ocemod.2019.01.003.
Pan, W., Kramer, S.C., Piggott, M.D., 2021. A sigma-coordinate non-hydrostatic discontinuous finite element coastal ocean model. Ocean Modelling 157, 1463–5003. URL: https://doi.org/10.1016/j.ocemod.2020.101732.
Pearson, B., Fox-Kemper, B., Bachman, S., Bryan, F., 2017. Evaluation of scale-aware subgrid mesoscale eddy models in a global eddy-rich mode. Ocean modelling 115, 42–58. URL: https://doi.org/10.1016/j.ocemod.2017.05.007.

Petersen, M., Jacobsen, D., Ringler, T., Hecht, M., Maltrud, M., 2015. Evaluation of the arbitrary Langrangian-Eulerian vertical coordinate method in the MPAS-ocean model. Ocean Modelling 86, 93–113. URL: https://doi.org/10.1016/j.ocemod.2014.12.004.

Ralston, D.K., Cowles, G.W., Geyer, W.R., Holleman, R.C., 2017. Turbulent and numerical mixing in a salt wedge estuary: Dependence on grid resolution, bottom roughness, and turbulence closure. Journal of Geophysical Research 122, 692–712. URL: https://doi.org/10.1002/2016JC011738.

Rennau, H., Burchard, H., 2009. Quantitative analysis of numerically induced mixing in a coastal model application. Ocean modelling 59, 671–687. URL: https://doi.org/10.1007/s10236-009-0201-x.

Robert, A.M., Kaper, H.G., 1986. Multiple time scale phenomena and numerical methods. Journal of computational physics 63, 241–256.

Saunders, P.M., 1973. The instability of a baroclinic vortex. Journal of Physical oceanography 3, 61–65. URL: https://doi.org/10.1175/1520-0485(1973)003%3C0061:TIOABV%3E2.0.CO;2.

Scholz, P., Lohmann, G., Wang, Q., Danilov, S., 2013. Evaluation of a finite-element sea-ice ocean model (fesom) set-up to study the interannual to decadal variability in the deep-water formation rates. Ocean modelling 63, 347—370. URL: https://doi.org/10.1007/s10236-012-0590-0.

Shchepetkin A.F., M.J., 2005. The regional oceanic modeling system (ROMS) a split-explicit, free-surface, topography-following-coordinate oceanic model. Ocean Modelling 9, 347–404. URL: https://doi.org/10.1016/j.ocemod.2004.08.002.

Song, Y., Haidvogel, D., 1994. A semi-implicit ocean circulation model using a generalized topography-following coordinate system. Journal of Computational Physics 115, 228–244. URL: https://doi.org/10.1006/jcph.1994.1189.

Tartinville, B., Deleersnijder, E., Lazure, P., Proctor, R., Ruddick, K.G., Uittenbogaard, R.E., 1998. A coastal ocean model intercomparison study for a three-dimensional idealised test case. Applied Mathematical Modelling 22, 165–182. URL: https://doi.org/10.1016/S0307-904X(98)00015-8.

Vallaeys, V., Lambrechts, J., Delandmeter, P., Pätsch, J., Spitzy, A., Hanert, E., Deleersnijder, E., 2021. Understanding the circulation in the deep, micro-tidal and strongly stratified congo river estuary. Ocean Modelling 167, 1463–5003. URL: https://doi.org/10.1016/j.ocemod.2021.101890.

Visbal, M.R., Gaitonde, D.V., 2002. A study of numerical dissipation in time-splitting methods for navier–stokes equations. Journal of Computational Physics 177, 1–29.

Weiss, L.B., Dahirel, V., Marry, V., Jardat, M., 2018. Computation of the hydrodynamic radius of charged nanoparticles from nonequilibrium molecular dynamics. The Journal of Physical Chemistry B 122 (22), 5940—5950. URL: https://doi.org/10.1021/acs.jpcb.8b01153.

White, L., Legat, V., Deleersnijder, E., 2007. Tracer conservation for the three-dimensional, finite-element,free-surface, ocean modeling on moving prismatic meshes. American Meteorological Society 136, 420–442. URL: https://doi.org/10.1175/2007MWR2137.1.

Wicker, L.J., Skamarock, W.C., 2002. Time-splitting methods for elastic models using forward time schemes. Monthly Weather Review 130, 2088–2097.

Zhang, Y., Ye, F., Stanev, E., Grashorn, S., 2016. Seamless cross-scale modeling with SCHISM. Ocean modelling 102, 64–81. URL: https://doi.org/10.1016/j.ocemod.2016.05.002.